The Nickel Site of *Bacillus pasteurii* UreE, a Urease Metallo-Chaperone, As Revealed by Metal-Binding Studies and X-ray Absorption Spectroscopy†

Massimiliano Stola,‡ Francesco Musiani,‡ Stefano Mangani,§,⊥ Paola Turano,||,⊥ Niyaz Safarov,‡ Barbara Zambelli,‡ and Stefano Ciurli*,‡,⊥

Laboratory of Bioinorganic Chemistry, Department of Agro-Environmental Science and Technology, University of Bologna, Viale Giuseppe Fanin 40, 40127 Bologna, Italy, Department of Chemistry, University of Siena, Via Aldo Moro 2, 53100 Siena, Italy, Department of Chemistry, University of Firenze, Via della Lastruccia 5, 50019 Sesto Fiorentino, Italy, and CERM (Center for Magnetic Resonance), Via Luigi Sacconi 6, 50019 Sesto Fiorentino, Italy

Received January 17, 2006; Revised Manuscript Received March 28, 2006

ABSTRACT: UreE is a homodimeric metallo-chaperone that assists the insertion of Ni^{2+} ions in the active site of urease. The crystal structures of UreE from *Bacillus pasteurii* and *Klebsiella aerogenes* have been determined, but the details of the nickel-binding site were not elucidated due to solid-state effects that caused disorder in a key portion of the protein. A complementary approach to this problem is described here. Titrations of wild-type *Bacillus pasteurii* UreE (*Bp*UreE) with Ni^{2+}, followed by metal ion quantitative analysis using inductively coupled plasma optical emission spectrometry (ICP-OES), established the binding of 2 Ni^{2+} ions to the functional dimer, with an overall dissociation constant $K_D = 35\ \mu M$. To establish the nature, the number, and the geometry of the ligands around the Ni^{2+} ions in *Bp*UreE-Ni_2, X-ray absorption spectroscopy data were collected and analyzed using an approach that combines ab initio extended X-ray absorption fine structure (EXAFS) calculations with a systematic search of several possible coordination geometries, using the Simplex algorithm. This analysis indicated the presence of Ni^{2+} ions in octahedral coordination geometry and an average of two histidine residues and four O/N ligands bound to each metal ion. The fit improved significantly with the incorporation, in the model, of a Ni−O−Ni moiety, suggesting the presence of a hydroxide-bridged dinuclear cluster in the Ni-loaded *Bp*UreE. These results were interpreted using two possible models. One model involves the presence of two identical metal sites binding Ni^{2+} with negative cooperativity, with each metal ion bound to the conserved His^{100} as well as to either His^{145} or His^{147} from each monomer, residues found largely conserved at the C-terminal. The alternative model comprises the presence of two different binding sites featuring different affinity for Ni^{2+}. This latter model would involve the presence of a dinuclear metallic core, with one Ni^{2+} ion bound to one His^{100} from each monomer, and the second Ni^{2+} ion bound to a pair of either His^{145} or His^{147}. The arguments in favor of one model as compared to the other are discussed on the basis of the available biochemical data.

The structural details of the mechanisms by which specific metal ions are transported in the cell and inserted into the correct metallo-enzyme have been the subject of recent investigations. This process must be very specific; indeed, many transition metals are essential but may also constitute potential risks of high toxicity if they bind to the wrong cellular components, hampering their function. A class of soluble metal-binding proteins, known as metallo-chaperones, has been established as being fundamental for this process (*1*, *2*), and molecular information has been collected on copper (*3*), zinc (*4*), iron (*5*), and manganese (*6*) chaperones. Related proteins are involved in nickel metabolism (*7*). This paper deals with the elucidation of the metal-binding properties of UreE, a nickel-chaperone involved in the in vivo assembly of urease, a nickel-containing enzyme that catalyzes urea hydrolysis in the last step of nitrogen mineralization (*8*, *9*). This process requires four accessory proteins, named UreD, UreE, UreF, and UreG (*10*, *11*), but the specific functions of these proteins are not fully understood. UreD appears to be a specific chaperone that facilitates nickel insertion into apo-urease by stabilizing a proper protein conformation (*12*). UreG is a Zn-binding dimeric GTPase that is intrinsically unstructured in solution (*13*) and possibly involved in an energy-dependent step during in vivo urease assembly (*14*, *15*). UreG and UreF form a super-complex with the UreD−apourease complex (*16*), suggesting that such large aggregates could be required

† This work was supported by Grants PRIN-2001 and PRIN-2003 from the Ministero Italiano dell'Università e della Ricerca (MIUR) and by the European Community Contract No. RII3/CT/2004/5060008 for the work performed at EMBL Hamburg. M.S., F.M., and N.S. are recipients of fellowships from Consorzio Interuniversitario di Risonanze Magnetiche di Metalloproteine Paramagnetiche (CIRMMP). B.Z. is the recipient of a Ph.D. fellowship from the University of Bologna.

* Corresponding author: Stefano Ciurli, Laboratory of Bioinorganic Chemistry, Department of Agro-Environmental Science and Technology, University of Bologna, Viale Giuseppe Fanin 40, 40127 Bologna, Italy. Phone, +39-051-209-6204; fax, +39-051-209-6203; e-mail, stefano.ciurli@unibo.it.

‡ University of Bologna.

§ University of Siena.

|| University of Firenze.

⊥ CERM (Center for Magnetic Resonance).

10.1021/bi0601003 CCC: $33.50
Published on Web 04/28/2006

for in vivo activation of urease (*15*). Finally, UreE binds nickel and is thought to interact with the UreDFG−apourease super-complex facilitating Ni^{2+}-incorporation in the urease active site (*17*−*22*).

The metal-binding properties of UreE have been the subject of numerous investigations, but a general and definitive picture is still not available. The first of these studies dates back to 1993, when it was discovered that UreE from *Klebsiella aerogenes* (*Ka*UreE)[1] possesses a His-rich C-terminus (10 histidines out of the last 15 residues). This protein was able to bind 6.05 ± 0.25 Ni atoms per functional dimer in a coordination environment of 3−5 histidines, with a macroscopic average K_D of 9.6 ± 1.3 μM (*18*). However, only a small portion of all UreE proteins feature such a long His-rich C-terminus region (*23*, *24*), and therefore, the properties of wild-type *Ka*UreE cannot be taken as representative of the entire class of UreEs. The Ni^{2+}-binding properties of a truncated form of *Ka*UreE, lacking the last 15 residues of the His-rich C-terminal portion of the protein, and named H144* *Ka*UreE, were reported in 1996 (*19*). The data were interpreted as indicating the binding of 1.9 ± 0.2 Ni atoms to H144* *Ka*UreE, but could not be fitted to a simple model that assumed the presence of independent sites with identical binding affinities, and cooperativity was included. This treatment yielded the values for the first and second binding constants (K_{D1} = 85 ± 10 and K_{D2} = 0.78 ± 0.1 μM, respectively), indicating a positive cooperativity in the binding of the two Ni^{2+} ions. The macroscopic dissociation constant K_D was estimated as ca. 8 μM. The physiological activity of H144* *Ka*UreE was reported to be about 20% lower than that of the wild-type *Ka*UreE (*19*). In 1998, X-ray absorption data on the truncated H144* *Ka*UreE were interpreted with a model involving two Ni^{2+} ions bound by N/O donors in pseudo-octahedral five- or six-coordinate sites. The two metal ions appeared to be spectroscopically distinguishable, with one Ni^{2+} bound to ≥3 His and the other bound to ≥2 His (*20*). In 1999, site-specific mutagenesis experiments performed on H144* *Ka*UreE were described, and mutants were tested to identify the residues responsible for the binding of nickel (*21*). In this study, an improved fitting procedure was used to show that H144* *Ka*UreE binds 2.01 Ni^{2+} ions with K_{D1} = 47 μM and K_{D2} = 1.5 μM, with positive cooperativity (Hill coefficient = 1.69) and average macroscopic binding constant K_D = 8.6 μM. The first site was reported to involve His^{96}, His^{112}, Asp^{111}, and Cys^{79}, while the second site appeared to contain His^{110}. However, only His^{96} and Asp^{111} were critically involved in Ni^{2+} incorporation into the urease active site (*21*, *22*, *25*).

In 2001, the crystal structure of H144* *Ka*UreE was reported, and the striking presence of three, and not two, metal-binding sites was detected by soaking the crystal of the apo-form in a copper-containing solution (*26*), contradicting all the previous studies of the stoichiometry of metal binding to this protein. The authors explained this incongruity as resulting from an aberrant reactivity of H144* *Ka*UreE with protein assay reagents, with the consequent overestimation of the protein concentration and therefore decrease of the calculated binding stoichiometry (*26*). Of these three binding sites, two were located on identical positions of each monomer of the homodimeric protein, related by symmetry, and involved the presence of His^{110} and His^{112}, while the third site was at the interface of the two monomers and involved His^{96} (Figure 1A). The topology and the coordination environment of the three metal-binding sites revealed by the structure of H144* *Ka*UreE explained the fact that the mutants His^{110}/Ala and His^{112}/Ala bind only a single Ni^{2+} ion (presumably at the His^{96} site) and that the mutant His^{96}/Ala binds two Ni^{2+} ions (in the two His^{110}−His^{112} symmetric sites) (*21*). The last few residues at the C-termini of *Ka*UreE could not be located in the structure, due to their disordered positions in the solid state.

The structure of *Bacillus pasteurii* UreE (*Bp*UreE) was also concomitantly and independently reported in 2001 (*27*). *Bp*UreE and *Ka*UreE share many structural features (*24*) but differ in the fact that the His^{110}−His^{112} binding site present in *Ka*UreE is absent in *Bp*UreE due to the natural replacement of these two nonconserved histidines by a tyrosine and a lysine, respectively (Figure 1B). In addition, while *Ka*UreE is present as the functional dimer in the crystal, *Bp*UreE crystallizes as a dimer of dimers, bridged by a single Zn^{2+} ion bound to four His^{100} (fully conserved residues corresponding to His^{96} in *Ka*UreE), at the interface of two monomers, with each His^{100} provided by one of the four UreE monomers. The result is that the metal-binding site in the functional dimer of *Bp*UreE is strongly altered due to such aggregation, and in particular, as found in *Ka*UreE but for different reasons, the C-termini are disordered in the crystal, and not visible.

In the cases represented by UreE sequences containing a His-rich C-terminus, the protein could have a dual role, both as nickel storage and as nickel delivery device. Under this assumption, UreE would use the His-rich C-terminus, when present, to scoop up Ni^{2+} from the cytoplasm and to store it in a high-affinity site, as previously suggested (*18*). In instances where a long His-rich C-terminus is not present, as in the case of *B. pasteurii*, other proteins may carry out this activity; for instance, a study on UreE from *Helicobacter pylori* has demonstrated that the addition of a His-rich fragment to the C-terminus of *Hp*UreE, which normally does not contain it, can complement the nickel-transport deficiency observed in mutant strains lacking *hypA* and *hypB*, genes that code for Ni,Fe-hydrogenase accessory proteins (*28*).

The direct or indirect involvement of the C-terminal portion of UreE in the binding of nickel was recently proposed for *Bp*UreE, and in particular, the role of His^{145} and His^{147} present in this region of the backbone was suggested based of the disappearance of their NMR signals upon binding of the paramagnetic (S = 1) high-spin Ni^{2+} ions (*29*), consistently with previous evidence for the presence of octahedral Ni^{2+} ions using paramagnetic ^1H NMR spectroscopy (*30*). This NMR study was complemented with a Ni-binding titration using equilibrium dialysis followed through the radioactivity of the ^{63}Ni isotope. The analysis of the stoichiometry and binding constants involved

[1] Abbreviations: ICP-OES, inductively coupled plasma optical emission spectrometry; XAS, X-ray absorption spectroscopy; EXAFS, extended X-ray absorption fine structure; NMR, nuclear magnetic resonance; OD_{600}, optical density at 600 nm; AMS, ammonium sulfate; MWCO, molecular weight cutoff; SDS−PAGE, sodium dodecyl sulfate−polyacrylamide gel electrophoresis; DLS, dynamic light scattering; DESY, Deutsches electronic synchrotron; EMBL, European molecular biology laboratory; XANES, X-ray absorption near-edge spectroscopy; MHz, megahertz; eV, electronvolt; PDB, protein data bank; *Bp*, *Bacillus pasteurii*; *Ka*, *Klebsiella aerogenes*; *Hp*, *Helicobacter pylori*.

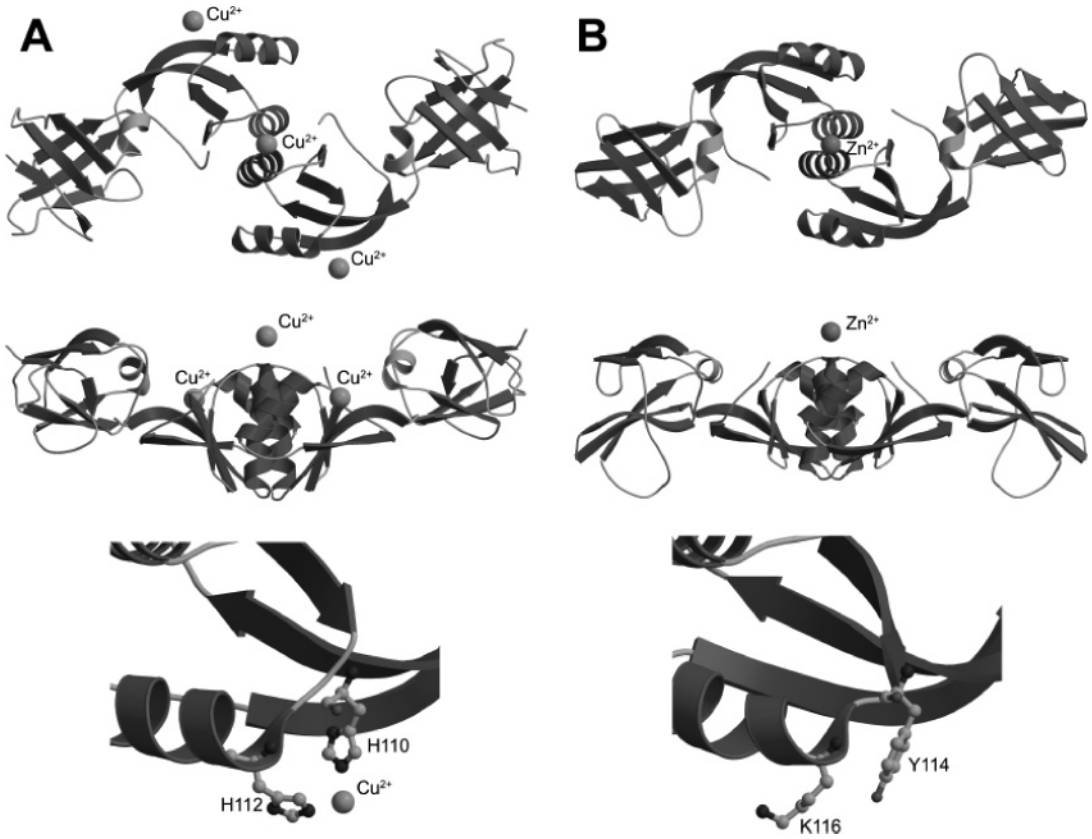

FIGURE 1: Ribbon schematic views of the dimer of *Ka*UreE (A) and *Bp*UreE (B), showing the binding sites for the metal ions (represented as spheres) detected by X-ray crystallography. The bottom panels show a close-up view of the nonfunctional metal-binding site in *Ka*UreE (A) and the corresponding protein region in *Bp*UreE (B), evidencing the different residues in the two cases.

the incorrect use of an equation for the data treatment: Figure 7 in the paper by Won et al. (*29*) reports a plot of bound Ni^{2+} (M_b) per *Bp*UreE dimer (fractional saturation) versus the total amount of nickel used to equilibrate with the protein (M_t), while the fit was performed using eq 1 in the paper, which contains the fractional saturation as a function of the free metal ion present in solution at equilibrium (M_f). The use of this equation led the authors to obtain saturation at 2.49 ± 0.05 Ni atoms per dimer with an average $K_D = 17.3 \pm 0.9$ μM. A comparison of the erroneously calculated data obtained on wild-type *Bp*UreE with analogous data obtained for the H91A mutant of H144* *Ka*UreE, which was reported to bind 2.02 Ni^{2+} ions (*21*) and later corrected as binding three Ni^{2+} ions on the basis of the crystal structure of the Cu-bound *Ka*UreE (*26*), led the authors to conclude that *Bp*UreE binds three Ni^{2+} per dimer, with one Ni^{2+} bound to His^{100}, and two Ni^{2+} to His^{145} and His^{147} (*29*).

In a continuing effort to characterize the proteins encoded by the urease operon in *B. pasteurii* (*13*, *24*, *27*, *30*−*38*), we report on a complementary study performed using inductively coupled plasma optical emission spectrometry (ICP-OES), as well as X-ray absorption spectroscopy (XAS), with the goal to establish the metal-binding stoichiometry, affinity, and structural features of the Ni-binding site of *Bp*UreE.

MATERIALS AND METHODS

Protein Purification. Cells of *Escherichia coli* BL21(DE3) (Novagen, Madison, WI) were transformed by electroporation with the pET-3d plasmid (Novagen, Madison, WI) containing the wild-type *Bp*UreE gene (pET-3d::*ureE*, Prof. Donald Bryant, Pennsylvania State University). The cells were grown in 3 L of M9 medium supplemented with ampicillin (100 μg mL^{-1}), at 37 °C with vigorous stirring. Expression was induced by addition of IPTG (isopropyl β-thiogalactopyranoside) to the final concentration of 0.4 mM when OD_{600} reached 0.8−0.9, overnight. The cells were harvested by centrifugation at 8000*g* for 10 min at 4 °C, and resuspended in 300 mL of 50 mM Tris-HCl, pH 7.5, containing 10 mM $MgCl_2$ and 20 μg mL^{-1} bovine pancreas DNAse-I. The cells were passed through a mixer homogenizer and subsequently broken by two passages through a French Pressure cell (SLM-Aminco) operating at 20 000 psi. Cell debris were removed by centrifugation at 12 000*g* for 30 min, at 4 °C. Solid ammonium sulfate (AMS, 40% saturation) was added to the extract, and the supernatant obtained by centrifugation (12 000*g* for 20 min) was further treated with AMS up to 60% saturation. The supernatant obtained after centrifugation as above was loaded onto a Phenyl-Sepharose XK26 column (Amersham-Pharmacia Biotech) preequilibrated with 50 mM Tris-HCl buffer, pH 7.5, containing 2 M AMS and 5 mM EDTA (ethylenediamine tetraacetic acid). The column was washed with the starting buffer until the baseline was straight, using a flow rate of 3 mL min^{-1}. A 500 mL linear gradient of 50 mM Tris-HCl buffer, pH 7.5, containing a decreasing concentration of AMS (from 2 to 1 M) was applied to elute UreE. Fractions containing UreE (eluted at about 1.6 M AMS) were combined and dialyzed (5 kDa molecular weight cutoff, MWCO membrane) against 50 mM Tris-HCl buffer, pH 7.5.

The resulting solution was applied onto a Q-Sepharose XK26 column (Amersham-Pharmacia Biotech) previously equilibrated with 50 mM Tris-HCl buffer, pH 7.5. After the column was washed with the equilibration buffer, a 500 mL linear gradient of NaCl was applied from 0 to 0.8 M at 3 mL min^{-1}. Fractions containing *Bp*UreE (eluted at about 0.2 M NaCl) were combined and concentrated using 5 kDa MWCO Amicon and Centricon ultra-filtration units (Millipore Corporation, Bedford, MA). The purified protein amounted to 0.20 g and was stored at −80 °C. Protein quantization was performed by absorption spectroscopy, using the theoretical value of the extinction coefficient $\epsilon_{280} = 21\,430\ M^{-1}\ cm^{-1}$ calculated using the amino acid sequence of the wild-type protein derived using the ProtParam program (http://us.expasy.org/cgi-bin/protparam).

The apparent molecular mass of *Bp*UreE in denaturing and nondenaturing conditions was estimated by SDS−PAGE and gel filtration chromatography as previously described (*30*). A small fraction (100 μL) of the obtained protein solution was applied to a Superdex-75 FPLC column (24 mL) conditioned with 50 mM Tris-HCl buffer, pH 7.5, containing 0.2 M NaCl buffer. SDS−PAGE was performed using a Bio-Rad Mini-Protean II apparatus (Richmond, CA) according to the method of Laemmli (*39*) in a 15% (w/v) acrylamide−bisacrylamide separating gel, stained using either Coomassie brilliant blue R-250 or Silver staining.

Metal-Binding Experiments. In all the following operations, care was taken to avoid exogenous metal contamination. Ni^{2+} nitrate solutions were prepared starting from ICP 1000 ppm standard solutions (CPI International, Santa Rosa, CA) diluted to 2 mM with 50 mM Tris-HCl buffer, pH 7.5, containing NaCl 0.5 M. Equal volumes of *Bp*UreE and metal solutions were mixed in 1:1 ratio to yield a constant concentration of protein (40 μM *Bp*UreE dimer) and an increasing concentration of metal ion. No precipitation was observed during the titration. The resulting mixtures were left overnight at 25 °C and then filtered by centrifugation using 0.5 mL Centricon (MWCO 5 kDa). No precipitation was observed during the concentration step. The filtered solution was diluted to 10 mL with milliQ water. Metal analysis was performed using a Spectro Ciros CCD ICP optical emission spectrometer (Spectro Analytical Instruments GmbH, Kleve, Germany) in combination with a Lichte nebulizer and a peristaltic pump for sample introduction. The ICP-OES system was calibrated by serial dilutions of appropriate single and multielement standards (CPI International, Santa Rosa, CA). The standardization curve was constructed with standard solutions of 0.1, 0.5, 1, and 5 mg L^{-1} of Ni in 1.7 mM Tris-HCl, pH 7.5, and 5 mM NaCl with a linear fitting. The reported concentrations were corrected with buffer blank. A radio frequency power of 1400 W, a nebulizer gas flow of 0.8 L min^{-1}, and a plasma gas flow of 14 L min^{-1} were used. The sample uptake was set at 2 mL min^{-1} for 24 s, and wash time of 15 s at 4 mL min^{-1} plus 45 s at 2 mL min^{-1}, for each sample. Quality control was established by evaluation of buffer containing standards. The 221.648 and 231.604 nm emission lines of Ni were used for analysis. The wavelength-averaged experimental points were fitted using the MacCurveFit software, and the fit was optimized using a Quasi-Newton algorithm. The minimized parameters were the sum of the square errors, SSE, and the correlation coefficient R^2. SSE is defined as

$$\mathrm{SSE} = \sum (y_i - f(x_i, a, b, c, \ldots))^2 \quad (1)$$

where x_i and y_i are the ith data pair in the data window, f is the function used for the fit, and a, b, c, and so forth, are the variable coefficients in the fit. R^2 is defined as

$$R^2 = 1 - \frac{n \cdot \mathrm{SSE}}{n \sum y_i^2 - (\sum y_i)^2} \quad (2)$$

where n is the number of data points. A perfect fit would have $\mathrm{SSE}_{min} = 0$ and $R^2_{max} = 1$, with the fit improving by decreasing SSE and increasing R^2.

Prior to all spectroscopic measurements, the metal-loaded protein samples were spun for 30 min using a Beckman AirFuge centrifuge operating at 25 000 psi. The aggregation state of the metal-bound protein was tested in the 50−250 μM concentration range in 50 mM Tris-HCl buffer, pH 7.5, containing 0.5 M NaCl, by dynamic light-scattering measurements using a DynaPro 99 DLS-instrument, and the data were analyzed using the *DYNAMICS* Version 5.24.02 from Protein Solutions software. Polydispersity was defined as (standard deviation of the particle size)/(average particle size), assuming a monomodal size distribution of the system.

X-ray Absorption Spectroscopy Data Collection. Samples for X-ray absorption experiments were prepared both in solution (Ni(Sol)) and as lyophilized material (Ni(Lyo)). For the solution sample, 50 μL of a 400 μM solution of Ni^{2+} nitrate salt in 50 mM Tris-HCl buffer, pH 7.5, containing 0.5 M NaCl, was added to 50 μL of a 200 μM *Bp*UreE solution in the same buffer, obtaining a 100 μM solution of *Bp*UreE−Ni_2. No precipitation was observed. The Ni(Lyo) sample was prepared as above but using 1 mL of each protein and metal solution, and subsequently lyophilizing the resulting 100 μM solution of *Bp*UreE−Ni_2. For the liquid samples, 45 μL of the above solutions were filled into plastic cells covered with Kapton windows. For the Ni(Lyo) sample, the lyophilized material was compressed into the same type of plastic cells and sealed using Kapton tape. Both the cells and the Kapton tape used for the windows were thoroughly washed with MilliQ water and absolute ethanol and then dried before use. The sample cells were mounted in a two-stage Displex cryostat (modified Oxford instruments) and kept at 20 K during the data collection.

X-ray absorption data were collected at the DESY/EMBL (Hamburg, Germany) bending magnet beam line D2, using Si(111) double monochromator for the measurement at the nickel edge. During the measurements, the DESY storage ring was operating under normal conditions (4.5 GeV, 90−140 mA). Ionization chambers in front and behind the sample were used to monitor the incident and transmitted beam intensity, respectively. The X-ray absorption data were recorded by measuring the Ni−K_α fluorescence, using a Canberra 13-element solid-state detector and variable energy step widths. In the X-ray absorption near-edge structure (XANES) and extended X-ray absorption fine structure (EXAFS) regions, steps of 0.3 and 0.5−1.2 eV were used, respectively.

X-ray Absorption Spectroscopy Data Processing. The same protocol was followed for both Ni(Lyo) and Ni(Sol) samples. The summation of the spectral scans was performed after

an absolute energy calibration obtained by recording known Bragg reflections of a Si(220) crystal in back reflection geometry following a reported procedure (*40*). The background was removed using the ATHENA software package (*41*), which implements the AUTOBK algorithm (*42*), a program that determines an empirical background spline based on a distinction between data and background in terms of Fourier components. The input parameter to AUTOBK that determines the maximum frequency of the background R_{bkg} was set to 1.0 Å. Edge-step data normalization was determined by a linear pre-edge subtraction and a regression of a quadratic polynomial beyond the edge. The difference between the pre-edge linear polynomial and the post-edge quadratic polynomial, extrapolated to the edge energy E_0, was used as the normalization constant in the definition of $\chi(E)$ as

$$\chi(E) = \frac{[\mu(E) - \mu_0(E)]}{\mu_0(E_0)} \quad (3)$$

The EXAFS signal $\chi(k)$ versus k is then obtained by conversion of the abscissa of $\chi(E)$ by the formula:

$$k = \frac{2m_e}{\hbar^2}\sqrt{E - E_0} \quad (4)$$

where m_e is the mass of the electron and $\hbar$ is the Planck constant divided by π.

X-ray Absorption Spectroscopy Data Analysis. A heuristic picture of the EXAFS signal involves the generation of a photoelectron by the absorption of an X-ray photon, the latter having sufficient energy to free a core electron into a state above the Fermi energy. The photoelectron thus propagates as a spherical wave and is scattered by the neighboring atoms according to single and multiple scattering paths. This scattering phenomenon causes the formation of interference wiggles overlapped onto a smooth background that would be observed in the case of an isolated absorber atom. The EXAFS signal, obtained by subtracting this atomic background from the total spectrum, can be described by the following EXAFS equation (*43*):

$$\chi(k) = \sum_j \frac{N_j {S_0}^2 F_j(k)}{kR_j^2} e^{-2k^2\sigma_j^2} e^{-2R_j/\lambda(k)} \sin(2kR_j + \delta_j(k)) \quad (5)$$

In this equation, k is the photoelectron wavenumber, defined as in eq 4, and j is the index for the j_{th} scattering path. Eq 5 contains terms that depend on the structural template used (R_j = the half path length; N_j = the multiplicity or degeneracy of the path; σ_j = the mean-square displacement (also known as Debye−Waller factor) of the distance between the absorbing atom and the neighboring atom for the single scattering path; ${S_0}^2$ = the many body correction, also known as passive electron reduction factor) and terms that depend on the atomic potentials ($F_i(k)$ = the effective scattering amplitude; $\delta_i(k)$ = the effective scattering phase shift; $\lambda(k)$ = the mean free path of the photoelectron). For each starting structural template, the program FEFF6 (*44*), which implements multiple-scattering path expansion (*45*, *46*), was used to apply eq 5 to calculate the scattering paths and the resulting EXAFS signal based on the given atomic positions.

Then, the program IFEFFIT (*47*) was used to perform a fit of the theoretical model onto the experimental EXAFS signal. The structural parameters determined in a fit to the data included a perturbation of the initially estimated value of the edge energy E_0 (ΔE_0), using the same value for all paths, the half-path length (R_j) to each set of atoms (using the same parameter for the entire set of atoms belonging to the histidine ring fragment, thus, keeping the ring rigid), and the value of the Debye−Waller factor for each type of atom (also here the same σ_j was used for the histidine fragment). The ${S_0}^2$ parameter was fixed to 1.0 for all paths, while the value of N_j was dictated by each particular structural template used.

Fits to the k^3-weighted EXAFS data were made in the $|\chi(R)|$ versus R function (R-space), obtained by Fourier-transforming the $\chi(k)$ versus k EXAFS signal (k-space) filtered using a Hanning window (sill = 1.0 Å^{-1}) to select data in the 2.0−12.0 Å^{-1} data range (Δk). The whole frequency distribution spectrum thus obtained was filtered using a Hanning window (sill = 0.1 Å) to select a fit range of 1.0−6.0 Å (ΔR). The resulting number of independent points is calculated as $N_{idp} = 2\Delta R\Delta k/\pi$. The IFEFFIT program was also made to adjust the background in the fit and report the correlation between the background and the structural-fit parameters. We found that this correlation was always less than 60%, indicating that the background was not significantly affecting the structural-fit parameters.

IFEFFIT performs the fit by minimizing the χ^2 function defined as

$$\chi^2 = \frac{N_{idp}}{N_{pts}\epsilon^2}\sum_{i=1}^{N_{pts}}\{[\mathrm{Re}(\chi_{data}(R_i) - \chi_{theo}(R_i))]^2 + [\mathrm{Im}(\chi_{data}(R_i) - \chi_{theo}(R_i))]^2\} \quad (6)$$

where Re and Im indicate the real and imaginary parts of the complex Fourier transforms of the data and theory, N_{pts} is the number of points in the fitting range of the $\chi(R)$ data, and ϵ is the measurement uncertainty, calculated as the root-mean-square value of $\chi(R)$ between 15 and 25 Å under the assumption that the error is evenly distributed in R-space.

IFEFFIT performs a statistical analysis (*48*) and outputs the goodness-of-fit parameters χ^2 (defined in eq 6), the reduced chi-square χ_ν^2 ($\chi_\nu^2 = \chi^2/\nu$, where $\nu = N_{idp} - N_{par}$ and N_{par} = number of parameters floating in the fit), and the R-factor, defined as

$$R = \sum_{i=1}^{N_{pts}} \frac{[\mathrm{Re}(\chi_{data}(R_i) - \chi_{theo}(R_i))]^2 + [\mathrm{Im}(\chi_{data}(R_i) - \chi_{theo}(R_i))]^2}{[\mathrm{Re}(\chi_{data}(R_i))]^2 + [\mathrm{Im}(\chi_{data}(R_i))]^2} \quad (7)$$

Template Structure Building Procedure. Three-dimensional starting metal-binding site templates were built using an octahedral coordination geometry and Ni-ligand bond distances of 2.0 Å. Histidines were modeled including also Cβ atoms in order to better evaluate which nitrogen (Nδ or Nϵ) is bound to the central nickel ion. In the text, His(Nδ)

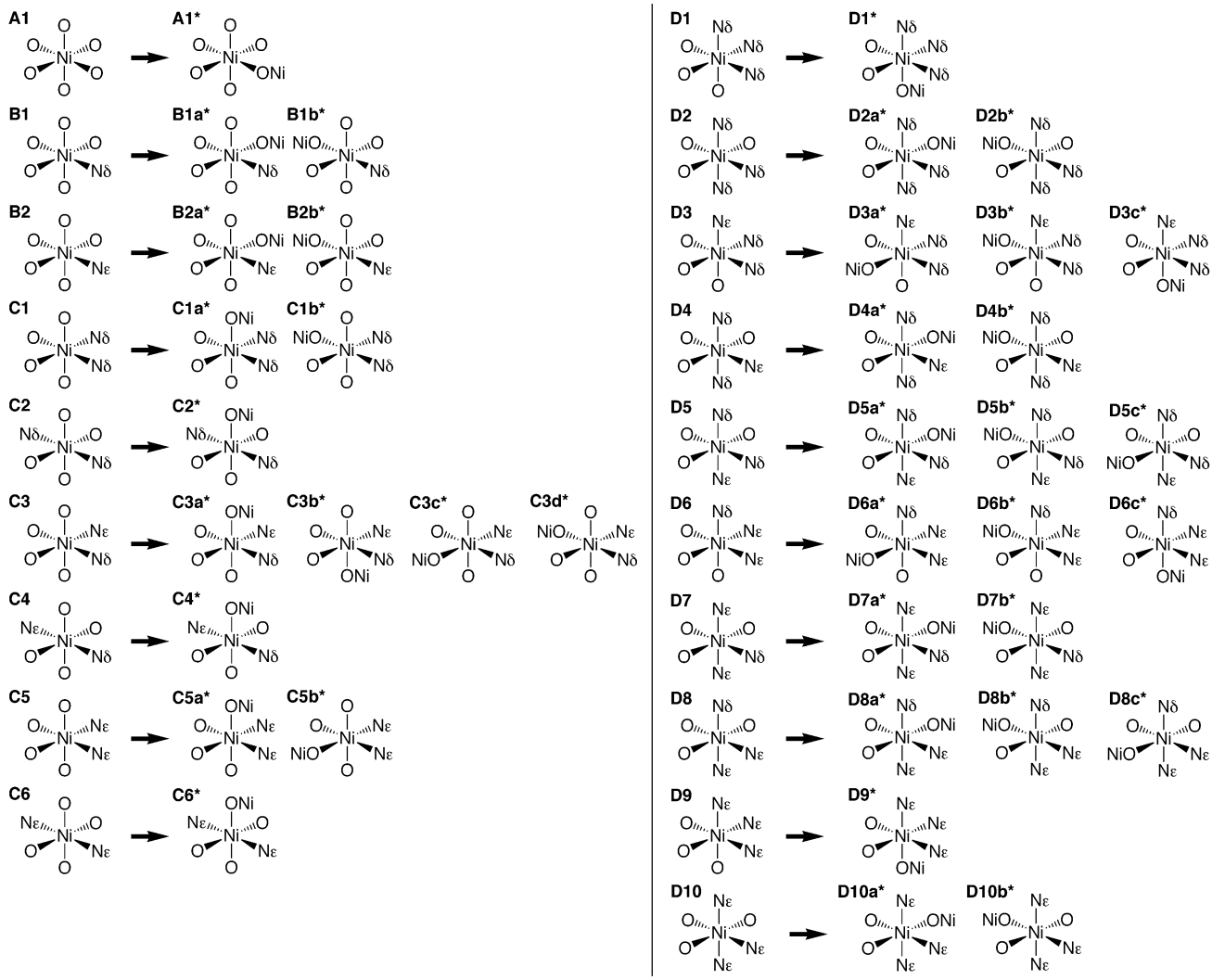

FIGURE 2: Schematic representations of the template models tested in the fits to the experimental EXAFS data. Nϵ and Nδ indicate histidine residues bound to the central nickel ion through the Nϵ and Nδ imidazole nitrogen atoms.

and His(Nϵ) are used to indicate a histidine bound to the central nickel ion by Nδ and Nϵ, respectively. Histidine side-chain bond lengths and angles were taken from Amber6 (*49*) Cornell parameters (*50*). All models studied in this work are reported in Figure 2.

Global Conformational Search for the Structural Parameters of the Nickel-Binding Site. For the simplest templates (**A**, **B**, **C**, **A***, and **B*** in Figure 2), a complete exploration of the conformational space was performed, trying to find the structure that best fits the experimental spectrum minimizing the *R*-factor described in eq 7. Histidines were manually rotated by 30° around the torsion angle X−Ni−His(Nϵ/δ)−His(Cϵ), while the −ONi group, when present in the template, was rotated by the same step around the torsion angle X−Ni−O−Ni. For each rotational conformer, five different values of the Ni−O−Ni angle were tried (95, 115, 135, 155, and 175°). In symmetric templates (e.g., **C2**) only unique conformations were tested, to avoid redundancy.

Simplex Implementation. For the templates corresponding to the **C***, **D**, and **D*** configurations, a home-developed program was used. The program reads an input file containing the atomic coordinates of the initial template and explores the conformation space using a downhill Simplex algorithm (*51*) coupled with FEFF6 (*44*) and IFEFFIT (*47*), to find the conformation that best fits the experimental spectra minimizing the *R*-factor described in eq 7. The algorithm is able to explore a multidimensional surface only by function evaluation (i.e., without derivatives evaluation), a strategy useful for the nonanalytical topology of the considered surfaces. For N given floating parameters defining an N-dimensional surface, a *simplex* is a geometrical figure consisting of $N + 1$ points (or vertices) and their interconnecting line segments. The downhill simplex method must start not just with a single point, but rather with $N + 1$ points, defining an initial simplex. A guess starting point for the *R*-factor is calculated as

$$R_0 = f(\phi_1, \phi_2, ..., \alpha) \quad (8)$$

where ϕ_i are the dihedral angles X−Ni−His(Nϵ/δ)−His(Cϵ) of histidines and the dihedral X−Ni−O−Ni angle of the −ONi group, while α is the angle Ni−O−Ni, giving a total of N dimensions. Then, the program obtains the initial simplex by calculating N additional *R*-factors by changing each floating parameter ϕ or α by an amount λ_i, the latter being a constant value for each parameter and representing the range in which each parameter will be explored by the simplex algorithm itself. Values of λ_ϕ and λ_α of 90° and 30° were used.

The downhill simplex then takes a series of steps, contracting, expanding, or reflecting simplex points, in order to explore the multidimensional parameter surface and to contract the simplex into a single minimum value of the *R*-factor. When the program finds a minimum of the *R*-factor, it restarts the simplex downhill search three times in order to determine if the found conformation is a local or global minimum. For every template tested, several starting conformers of each template were tried, to cover the entire conformational space.

Nuclear Magnetic Resonance Experiments. ^{15}N-enriched apo-*Bp*UreE was obtained as described above using a M9 medium supplemented with $(^{15}NH_4)_2SO_4$. The *Bp*UreE−Ni_2 sample was prepared by adding 300 μL of a 400 μM solution of Ni^{2+} nitrate salt in 50 mM Tris-HCl buffer, pH 7.5, containing 0.5 M NaCl to 300 μL of a 200 μM apo-*Bp*UreE solution in the same buffer. ^{15}N relaxation experiments were performed at 298 K using a Bruker Avance spectrometer operating at 500.13 MHz for the proton Larmor frequency, equipped with a cryoprobe. The pulse sequence used to obtain rates are those previously described (*52*−*57*) which include sensitivity enhancement and water suppression with the flip-back method. Nine time points were collected for the R_2 experiments, with variable delays taken in the range of 8−260 ms. Duplication of the measurements was performed to estimate the experimental uncertainty. A recycle delay of 2.2 s was used. In total, 2048 complex data points with 256 complex increments were collected.

All NMR spectra were processed with the XWINNMR program (Bruker) and analyzed with the Sparky v.3 (*58*) software. NMR relaxation data were fitted with the routine implemented in Sparky. A search routine was used within Sparky to find the positions of the peak maxima. The exponential decay curves for R_2 peak intensities were fitted to the two-parameter curve $h = Ae^{-Rt}$, where *h* is peak height and *t* is the variable delay parameter.

RESULTS

Purification of Wild-Type BpUreE. Wild-type *Bp*UreE was obtained by a modification of a previously reported protocol (*30*). The pET-3d::*ureE* plasmid used in this study expresses a protein that contains the correct five-residue fragment Y^{13}-ESSD at the N-terminus, instead of the fragment L^{13}SHQI present in the previously reported and studied *Bp*UreE (*27*, *30*). The use of a mineral medium to grow the transformed cells producing recombinant *Bp*UreE resulted in a significant increase of the amount of expressed protein. The purification procedure was consequently improved with respect to the previously published protocol that involved the use of Luria−Bertani medium (*30*), and only two chromatographic steps were needed after the initial ammonium sulfate precipitation. SDS−PAGE gels yielded a single band corresponding to the molecular mass of the monomer (ca. 17.5 kDa). The oligomerization state of the apo-protein in diluted solutions was monitored by size-exclusion chromatography experiments, which showed a single sharp peak corresponding to the mass of the dimeric form (ca. 35 kDa). For all measurements, buffers containing high salt concentration (0.5 M NaCl), known to be required to stabilize the protein fold and avoid protein aggregation (*59*), were used.

Metal-Binding Properties of BpUreE. The affinity of Ni^{2+} to *Bp*UreE was determined by measuring the concentration

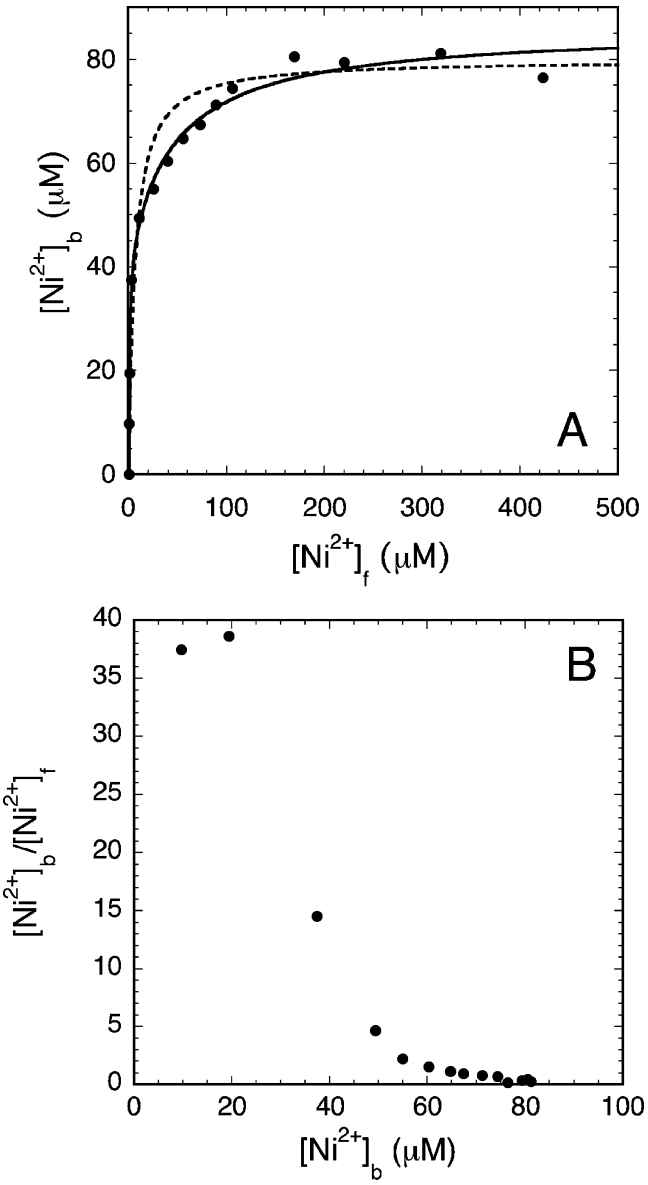

FIGURE 3: (A) Metal-binding titration curves for the interaction of 40 μM *Bp*UreE with Ni^{2+}. The dashed and continuous lines represent nonlinear curve fits using eqs 9 and 10A or 10B, respectively. (B) The Scatchard plot for the binding curve of *Bp*UreE to nickel is presented.

of the free ion resulting from the reaction of an increasing concentration of total ion to a fixed concentration of *Bp*UreE (40 μM functional dimer). The binding curve, obtained by reporting the amount of total bound metal (M_b) as a function of the total amount of Ni^{2+} added (M_t), shows saturation at ca. 80 μM, indicating that a maximum of two Ni^{2+} ions are bound to the *Bp*UreE dimer in the presence of excess metal. Figure 3A reports the amount of bound metal (M_b) as a function of the free ion at equilibrium (M_f).

Assuming a single-site binding model (that is, considering that the two Ni^{2+} ions show identical affinities for the two sites, homogeneous binding) the experimental points should follow a curve described by eq 9:

$$[M_b] = \frac{n[P_{tot}][M_f]}{K_D + [M_f]} \quad (9)$$

where P_t is the total concentration of the *Bp*UreE dimer, K_D

Scheme 1

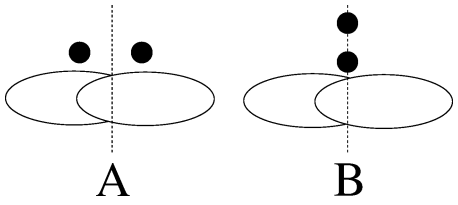

Scheme 2

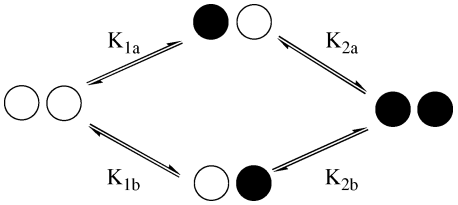

is the dissociation constant, and n is the number of binding sites (in our case, $n = 2$). The obtained best fit, reported in Figure 3A (dashed line), is clearly not satisfactory ($K_D = 3.6 \pm 1.1$ μM, SSE = 577.54; $R^2 = 0.94$). This observation suggests that the binding of the two Ni^{2+} ions is not homogeneous. The presence of two different populations of binding sites with different affinities is qualitatively confirmed by the nonlinearity of the Scatchard plot, which features an upward curvature determined by two intervening groups of points with different slopes (Figure 3B). Considering the fact that the protein is a homodimer with complete two-fold symmetry both in the solid state (*26*, *27*) and in solution (*29*), the simplest models involve the following two possibilities for the topology of the binding of the two Ni^{2+} ions to the *Bp*UreE dimer, summarized in Scheme 1A (Case A: two chemically identical sites with the different affinity resulting from binding cooperativity) and Scheme 1B (Case B: two chemically distinct sites, intrinsically binding the two Ni^{2+} ions with different affinities).

Case A: Identical Sites and Binding Cooperativity. In the Case A, a stepwise metal site loading mechanism would involve the equilibria shown in Scheme 2.

Considering Scheme 2 and the two-fold symmetric system, the following equalities involving the two different binding constants must be true: $K_{1a} = K_{1b} = K_1$ and $K_{2a} = K_{2b} = K_2$. As a consequence, the treatment of Scheme 1A using equilibrium theory yields the following eq 10A for the variation of the amount of bound metal ion (M_b) as a function of free ion at equilibrium (M_f):

$$[M_b] = 2[P_t]\frac{K_1[M_f] + K_1K_2[M_f]^2}{1 + 2K_1[M_f] + K_1K_2[M_f]^2} \quad (10A)$$

The best fit of the experimental points to eq 10A, shown in Figure 3A (solid line), is fully satisfactory ($R^2 = 0.993$; SSE = 65.2) and represents a significant improvement with respect to the use of a single constant as in eq 9. The binding constants obtained using this physical model are $K_1 = 0.73 \pm 0.11$ μM^{-1}, $K_2 = 0.04 \pm 0.01$ μM^{-1}. The resulting sequential dissociation constants are $K_{D1} = 1.4 \pm 0.2$ μM and $K_{D2} = 25 \pm 6$ μM. If this model is correct, the small Hill plot coefficient (0.46 using data points found between 25 and 75% saturation) derived from the Hill plot (*60*) would be interpreted as a confirmation that the second nickel ion binds with negative cooperativity.

Case B: Chemically Different Binding Sites. In Case B, the treatment of Scheme 1B using equilibrium theory yields the following eq 10B for the variation of the amount of bound metal ion (M_b) as a function of free ion at equilibrium (M_f):

$$[M_b] = [P_t]\frac{K_1[M_f] + 2K_1K_2[M_f]^2}{1 + K_1[M_f] + K_1K_2[M_f]^2} \quad (10B)$$

The best fit of the experimental points to eq 10B yields a curve identical to that obtained using eq 10A, with identical fit statistics. However, the calculated binding constants are $K_1 = 1.46 \pm 0.22$ μM^{-1}, $K_2 = 0.02 \pm 0.005$ μM^{-1}. The resulting sequential dissociation constants are $K_{D1} = 0.7 \pm 0.1$ μM and $K_{D2} = 50 \pm 12$ μM, respectively, corresponding to half and double the dissociation constants found using eq 10A. In this case, the Hill plot coefficient of 0.46 would be interpreted as a consequence of the intrinsic difference between the metal-binding affinities of the two sites and not as derived from negative binding cooperativity.

Regardless of the model used to interpret the metal binding data, the end point of the titration is reached upon addition of 2 equiv of nickel per *Bp*UreE functional dimer. Therefore, the samples of metal-bound *Bp*UreE for the subsequent spectroscopic studies were prepared using a dimer-to-metal ion concentration ratio of 1:2.

To avoid the oligomerization phenomena observed in the presence of metal ions at high protein concentrations (*30*), diluted solutions of *Bp*UreE−Ni_2 were prepared that allowed spectroscopic data with good signal-to-noise ratio to be obtained. The oligomerization state of the metal-loaded protein in these solutions was investigated both by dynamic light-scattering experiments, which yielded a single peak with a polydispersity value of 1.0 up to 250 μM protein concentration, and more precisely by NMR spectroscopy. In the latter case, ^{15}N transverse (R_2) relaxation rates were measured at 500.13 MHz for 100 μM solutions of the apoprotein and the *Bp*UreE−Ni_2 forms. Overlapping cross-peaks and signals with very low signal-to-noise ratio were not used in the dynamics analysis. The calculated average R_2 values were of the order of 20 s^{-1} for all cases, corresponding to correlation times of ca. 15 ns, typical for a protein of 30−35 kDa (*61*). These collective findings strongly support the idea that the protein (either in the apo- or metal-bound form) is present as the functional dimer in 100 μM solutions. This concentration was used for all the following spectroscopic measurements. Under these conditions, and using the equilibrium constants previously derived, it can be calculated that more than 90% of nickel is present in solution as bound metal.

X-ray Spectroscopic Studies. X-ray absorption spectra were initially acquired for 100 μM solutions of *Bp*UreE−Ni_2. The signal for this Ni(Sol) sample was weak ($\epsilon(R) = 0.370$) probably a consequence of combining the low concentration of the sample and the low fluorescence yield of Ni. For this reason, data were also collected on a lyophilized sample of *Bp*UreE−Ni_2, (Ni(Lyo) sample), which yielded a more satisfactory signal-to-noise ratio ($\epsilon(R) = 0.133$). The normalized Ni−K edge XANES spectra of the two types of samples of *Bp*UreE−Ni_2, Ni(Lyo) and Ni(Sol), reported in Figure

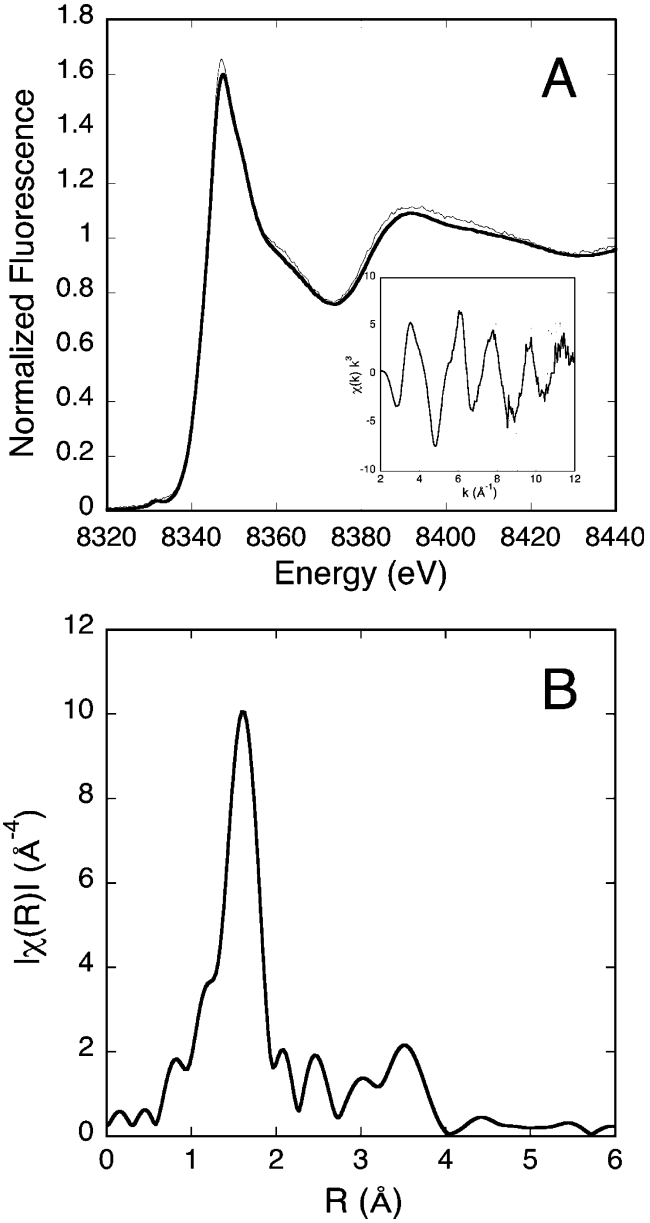

FIGURE 4: (A) Normalized X-ray fluorescence spectra in the Ni K-edge region for *Bp*UreE−Ni_2 in solution (Ni(Sol), thin line) and in the lyophilized state (Ni(Lyo), thick line). The corresponding k^3-weighted $\chi(k)$ EXAFS signals are shown in the figure inset. Processing parameters for Ni(Lyo): E_0 = 8344.6 eV; pre-edge regression in the range −150 to −30 eV below E_0; post-edge normalization range +150 to +784 eV above E_0; normalization constant = 0.90; spline range, 0.952−884 eV above E_0. Processing parameters for Ni(Sol): E_0 = 8344.6 eV; pre-edge regression in the range −109 to −30 eV below E_0; post-edge normalization range, +150 to +850 eV above E_0; normalization constant = 0.03; spline range, 0.952−950 eV above E_0. (B) Magnitude of Fourier transform of the k^3-weighted EXAFS data for *Bp*UreE−Ni_2 in the lyophilized state. The Hanning window (sill = 1.0 $Å^{-1}$ in k-space) was used to select data in the 2.0−12.0 $Å^{-1}$ data range.

4A, show that the pre-edge and edge regions do not depend on the physical state of the sample.

The absorption edge occurs at 8344.6 eV in both cases, which is appropriate for the presence of Ni^{2+} ions bound to N/O ligands (*62*). The binding of Ni^{2+} ions to 2nd-period elements is also confirmed by the intensity and the shape of the white line (maximum of the absorption at ca. 8348 eV), which is an independent indication of the type of the nickel ligands. Its intensity depends on the 'hard' (N/O) or 'soft' (RS^-/Cl^-) character of the donors to Ni^{2+} ions (*62*). The very low area ($1.9(2) \times 10^{-2}$ eV) of the pre-edge absorption, located at about 8332 eV, is indicative of a nearly centrosymmetric environment for the Ni^{2+} ions in both *Bp*UreE−Ni_2 samples (*62*). The pre-edge peak is in general assigned to a formally forbidden 1s−3d electronic transition of Ni^{2+}, with the transition probability increasing as the 3d−4p mixing of the metal orbitals increases going from square planar to octahedral to tetrahedral geometry of Ni^{2+}. The pre-edge absorption observed in the two *Bp*UreE−Ni_2 samples is lower than that observed in native urease, where the average nickel site has a geometry between distorted octahedral and square pyramidal (*32*, *34*, *63*). Neither spectrum shows a peak nor a shoulder near 8338 eV (assigned to a $1s \rightarrow 4p_z$ transition with shakedown contributions), expected in the presence of planar, four-coordinate Ni^{2+} centers (*62*).

In conclusion, all the evidence from the pre-edge and edge analysis points to the presence, in *Bp*UreE−Ni_2, of Ni^{2+} ions bound to a set of O/N donor atoms arranged in an octahedral geometry. It is worth noticing the strict similarity between the *Bp*UreE−Ni_2 pre-edge and edge data to the analogous data reported for H144**Ka*UreE−Ni (*20*), which suggests a very similar environment for the Ni^{2+} ions in the two proteins. The similarity extends also to the edge of the full-length *Ka*UreE reported earlier (*18*), even though the pre-edge feature appears somewhat higher in this case with respect to both H144**Ka*UreE−Ni and *Bp*UreE−Ni_2. The data obtained on the Ni(Lyo) sample, characterized by a high signal-to-noise ratio, were used for the subsequent structural analysis, which should be considered valid also for the Ni-(Sol) sample due to the identity of the Ni(Sol) and Ni(Lyo) edge region of the spectra (Figure 4A), extending also to the EXAFS region (inset of Figure 4A).

The Fourier transform of the Ni(Lyo) sample (shown in Figure 4B) features a strong first-shell peak in addition to higher shell features typical for the presence of histidine residues coordinated to the scattering metal ion. These higher shell peaks are reflected in the EXAFS spectrum as characteristic camelback features at ca. 4.0 and 5.5 $Å^{-1}$ (inset of Figure 4A).

A global conformational search was performed to fit the EXAFS data using the initial structural templates described in Figure 2. For EXAFS problems where the geometry is not known, several models should be selected for evaluations that encompass the set of reasonably possible structural conformations, and each should be examined separately. A proposed solution to this problem entails the generation of a large number of possible structural models followed by a statistical analysis of the fits (*64*). The presently used approach allows us to additionally implement a minimization criterion to guide the choice of the structural models used in each fit. This criterion is based on the well-known Simplex algorithm for the exploration of multidimensional parameter surfaces. The use of three-dimensional fitting models allows us to take in full account all the possible multiple scattering pathways and, in particular, those involving scattering between groups of atoms belonging to different metal ligands. The results of these fits are reported in Table 1. Calculations were also performed for the pairs of chiral models C3a*/C3b*, D3a*/D3b*, D5a*/D5c*, D6b*/D6c*, and D8a*/D8c* in order to check the consistency and robustness of the

Table 1: Statistical Parameters Obtained by Fitting the Fourier-Transformed EXAFS Spectra of *Bp*UreE−Ni_2 Using the Models Reported in Figure 2 and the Fitting Protocol Described in the Text[a]

model	χ^2	$\chi_\nu^2(R)$	N_{idp}	N_{var}	ν	R (%)	ΔE_0 (eV)	r(His) (Å)	r(O) (Å)	r(ONi) (Å)	σ^2(His) (Å^2)	σ^2(O) (Å^2)	σ^2(ONi) (Å^2)
A1	556.9	20.1	31	3	28	7.40	−5.944	-	2.063(7)	-	-	0.0069(6)	-
B1	262.2	10.2	31	5	26	3.48	−3.659	2.075(15)	2.068(7)	-	0.0025(17)	0.0068(7)	-
B2	236.4	9.2	31	5	26	3.14	−3.697	2.080(12)	2.067(7)	-	0.0007(14)	0.0076(8)	-
C1	379.7	14.8	31	5	26	5.04	−3.525	2.045(22)	2.071(7)	-	0.0084(24)	0.0034(5)	-
C2	361.5	14.1	31	5	26	4.80	−3.421	2.039(22)	2.072(6)	-	0.0085(24)	0.0033(5)	-
C3	353.9	13.8	31	5	26	4.70	−3.287	2.046(20)	2.074(7)	-	0.0074(25)	0.0034(6)	-
C4	335.5	13.0	31	5	26	4.46	−3.222	2.042(21)	2.074(6)	-	0.0077(24)	0.0034(5)	-
C5	348.0	13.5	31	5	26	4.62	−3.093	2.048(20)	2.075(7)	-	0.0069(22)	0.0035(6)	-
C6	336.2	13.1	31	5	26	4.46	−3.031	2.039(20)	2.076(6)	-	0.0069(22)	0.0033(5)	-
D1	253.8	9.9	31	5	26	3.34	−1.764	2.083(16)	2.073(6)	-	0.0092(15)	0.0031(6)	-
D2	326.1	12.7	31	5	26	4.33	−1.798	2.073(19)	2.076(7)	-	0.0088(17)	0.0032(7)	-
D3	274.8	10.7	31	5	26	3.65	−1.804	2.076(16)	2.075(7)	-	0.0081(15)	0.0034(7)	-
D4	296.9	11.5	31	5	26	3.94	−1.722	2.072(17)	2.078(7)	-	0.0081(16)	0.0034(8)	-
D5	286.6	11.1	31	5	26	3.81	−1.774	2.072(17)	2.078(7)	-	0.0082(16)	0.0033(7)	-
D6	254.5	9.9	31	5	26	3.38	−1.664	2.073(15)	2.078(7)	-	0.0076(14)	0.0036(7)	-
D7	267.8	10.4	31	5	26	3.56	−1.751	2.072(17)	2.078(7)	-	0.0078(15)	0.0034(8)	-
D8	261.0	10.1	31	5	26	3.47	−1.661	2.074(16)	2.078(7)	-	0.0078(15)	0.0035(8)	-
D9	252.6	9.8	31	5	26	3.35	−1.626	2.075(16)	2.078(7)	-	0.0074(14)	0.0037(8)	-
D10	276.5	10.7	31	5	26	3.67	−1.460	2.070(17)	2.081(8)	-	0.0074(15)	0.0036(8)	-
A1*	401.3	15.6	31	5	26	5.33	−7.059	-	2.059(6)	1.852(38)	-	0.0048(5)	0.0194(65)
B1a*	233.8	9.9	31	7	24	3.10	−4.196	2.023(20)	2.081(9)	2.037(25)	0.0046(21)	0.0047(9)	0.0041(24)
B1b*	248.7	10.5	31	7	24	3.30	−4.300	2.017(21)	2.079(9)	2.029(35)	0.0045(22)	0.0040(8)	0.0059(36)
B2a*	219.5	9.3	31	7	24	2.92	−3.575	2.117(18)	2.078(10)	2.022(14)	0.0035(20)	0.0067(9)	0.0066(20)
B2b*	238.0	10.0	31	7	24	3.16	−4.116	2.015(21)	2.081(9)	2.038(31)	0.0030(21)	0.0042(9)	0.0050(31)
C1a*	121.1	5.1	31	7	24	1.61	−3.028	2.046(14)	2.070(5)	2.097(16)	0.0078(14)	0.0039(6)	0.0059(15)
C1b*	185.7	7.8	31	7	24	2.47	−2.679	2.055(16)	2.061(8)	2.127(23)	0.0068(17)	0.0039(9)	0.0032(21)
C2*	175.9	7.4	31	7	24	2.34	−2.801	2.053(16)	2.063(9)	2.118(22)	0.0072(17)	0.0041(9)	0.0033(20)
C3a*	97.3	4.1	31	7	24	1.29	−2.673	2.050(12)	2.068(9)	2.112(17)	0.0066(14)	0.0043(9)	0.0057(17)
C3b*	95.1	4.0	31	7	24	1.26	−2.954	2.048(12)	2.069(5)	2.111(15)	0.0068(13)	0.0040(5)	0.0062(14)
C3c*	149.5	6.3	31	7	24	1.98	−2.551	2.053(13)	2.062(7)	2.138(18)	0.0062(13)	0.0039(8)	0.0027(15)
C3d*	149.6	6.3	31	7	24	1.99	−2.539	2.053(14)	2.062(7)	2.139(20)	0.0059(14)	0.0038(9)	0.0030(18)
C4*	142.9	6.0	31	7	24	1.90	−2.828	2.052(14)	2.065(8)	2.114(19)	0.0060(14)	0.0047(9)	0.0031(18)
C5a*	87.1	3.7	31	7	24	1.16	−2.806	2.048(12)	2.069(5)	2.116(14)	0.0062(12)	0.0040(5)	0.0059(14)
C5b*	128.2	5.4	31	7	24	1.70	−2.508	2.052(14)	2.062(8)	2.144(19)	0.0060(15)	0.0047(9)	0.0031(18)
C6*	127.3	5.4	31	7	24	1.69	−2.641	2.050(13)	2.064(7)	2.128(18)	0.0053(13)	0.0045(9)	0.0029(16)
D1*	206.2	8.7	31	7	24	2.74	−1.736	2.069(14)	2.058(9)	2.131(23)	0.0083(13)	0.0020(9)	0.0024(23)
D2a*	216.7	9.1	31	7	24	2.88	−0.323	2.107(15)	2.045(11)	2.163(19)	0.0046(12)	0.0022(14)	0.0051(16)
D2b*	204.0	8.6	31	7	24	2.71	−1.577	2.070(15)	2.058(10)	2.134(22)	0.0085(14)	0.0018(10)	0.0026(20)
D3a*	178.2	7.5	31	7	24	2.37	−1.739	2.067(13)	2.061(9)	2.128(22)	0.0077(12)	0.0023(8)	0.0030(20)
D3b*	180.5	7.6	31	7	24	2.40	−1.588	2.070(13)	2.057(8)	2.140(20)	0.0078(12)	0.0018(9)	0.0025(18)
D3c*	176.9	7.5	31	7	24	2.35	−1.661	2.069(14)	2.058(9)	2.136(22)	0.0077(12)	0.0023(9)	0.0029(20)
D4a*	181.0	7.6	31	7	24	2.40	−1.687	2.066(13)	2.062(9)	2.128(22)	0.0077(13)	0.0022(10)	0.0031(20)
D4b*	181.1	7.6	31	7	24	2.41	−1.589	2.069(14)	2.056(10)	2.139(21)	0.0080(13)	0.0018(10)	0.0024(19)
D5a*	183.1	7.7	31	7	24	2.43	−1.474	2.067(14)	2.060(8)	2.139(21)	0.0078(13)	0.0018(9)	0.0028(19)
D5b*	172.1	7.2	31	7	24	2.28	−1.751	2.066(14)	2.061(10)	2.127(21)	0.0078(13)	0.0022(10)	0.0028(19)
D5c*	183.4	7.7	31	7	24	2.43	−1.479	2.068(14)	2.058(9)	2.138(21)	0.0078(13)	0.0019(9)	0.0023(18)
D6a*	165.3	7.0	31	7	24	2.20	−1.489	2.064(11)	2.061(8)	2.145(18)	0.0072(11)	0.0024(8)	0.0022(19)
D6b*	160.1	6.7	31	7	24	2.13	−1.591	2.064(13)	2.065(10)	2.126(22)	0.0071(11)	0.0026(11)	0.0028(21)
D6c*	153.3	6.5	31	7	24	2.04	−1.551	2.068(12)	2.057(9)	2.141(19)	0.0072(11)	0.0020(9)	0.0020(18)
D7a*	162.6	6.9	31	7	24	2.16	−1.503	2.067(13)	2.060(8)	2.144(20)	0.0072(12)	0.0018(9)	0.0026(17)
D7b*	152.6	6.4	31	7	24	2.03	−1.623	2.067(13)	2.057(8)	2.143(18)	0.0074(11)	0.0018(9)	0.0023(16)
D8a*	154.4	6.5	31	7	24	2.05	−1.422	2.064(13)	2.062(8)	2.145(19)	0.0071(11)	0.0018(8)	0.0027(17)
D8b*	155.8	6.6	31	7	24	2.07	−1.465	2.065(13)	2.059(8)	2.15(18)	0.0073(12)	0.0015(9)	0.0021(16)
D8c*	161.1	6.8	31	7	24	2.14	−1.551	2.067(13)	2.069(8)	2.144(19)	0.0072(12)	0.0018(8)	0.0026(17)
D9*	150.7	6.3	31	7	24	2.00	−1.400	2.065(12)	2.061(7)	2.152(18)	0.0066(11)	0.0017(8)	0.0023(16)
D10a*	141.1	5.9	31	7	24	1.87	−1.506	2.065(12)	2.060(7)	2.148(18)	0.0067(11)	0.0019(8)	0.0024(15)
D10b*	148.5	6.2	31	7	24	1.97	−1.442	2.065(12)	2.060(8)	2.149(18)	0.0068(11)	0.0017(9)	0.0021(15)

[a] The resulting structural parameters are also reported.

obtained results, which was confirmed by the very small differences found for the statistical parameters within each pair (Table 1). Initially, the octahedral templates were constituted only by a central nickel ion, oxygen atoms, and histidines side chains (i.e., imidazole rings plus Cβ). Figure 5 reports the experimental Fourier-transformed EXAFS data compared with best simulated Fourier transforms for models including zero (**A**), one (**B**), two (**C**), and three (**D**) histidines. Template **A** was used merely for reference purposes, as the fit statistical parameters are as high as expected ($\chi_\nu^2(R)$ = 20.1, R-factor = 7.4%). In particular, template **A** fails in the simulation of the region between 2.0 and 4.0 Å. Simulations carried out using templates **B**, **C**, and **D** are characterized by an evident improvement of the fit in this region and a significant progress in the statistical parameters. The values for $\chi_\nu^2(R)$ range from 9.2 to 10.2 for model **B**, from 13.0 to 14.8 for model **C**, and from 9.8 to 12.7 for model **D**. General improvements in the simulated Fourier transform are evident in the peak located at about 2.5 Å. However, the peaks at about 3.0 and 3.5 Å are not fitted with sufficient accuracy, revealing discrepancies in the relative magnitude of such peaks. Moreover, simulated back-

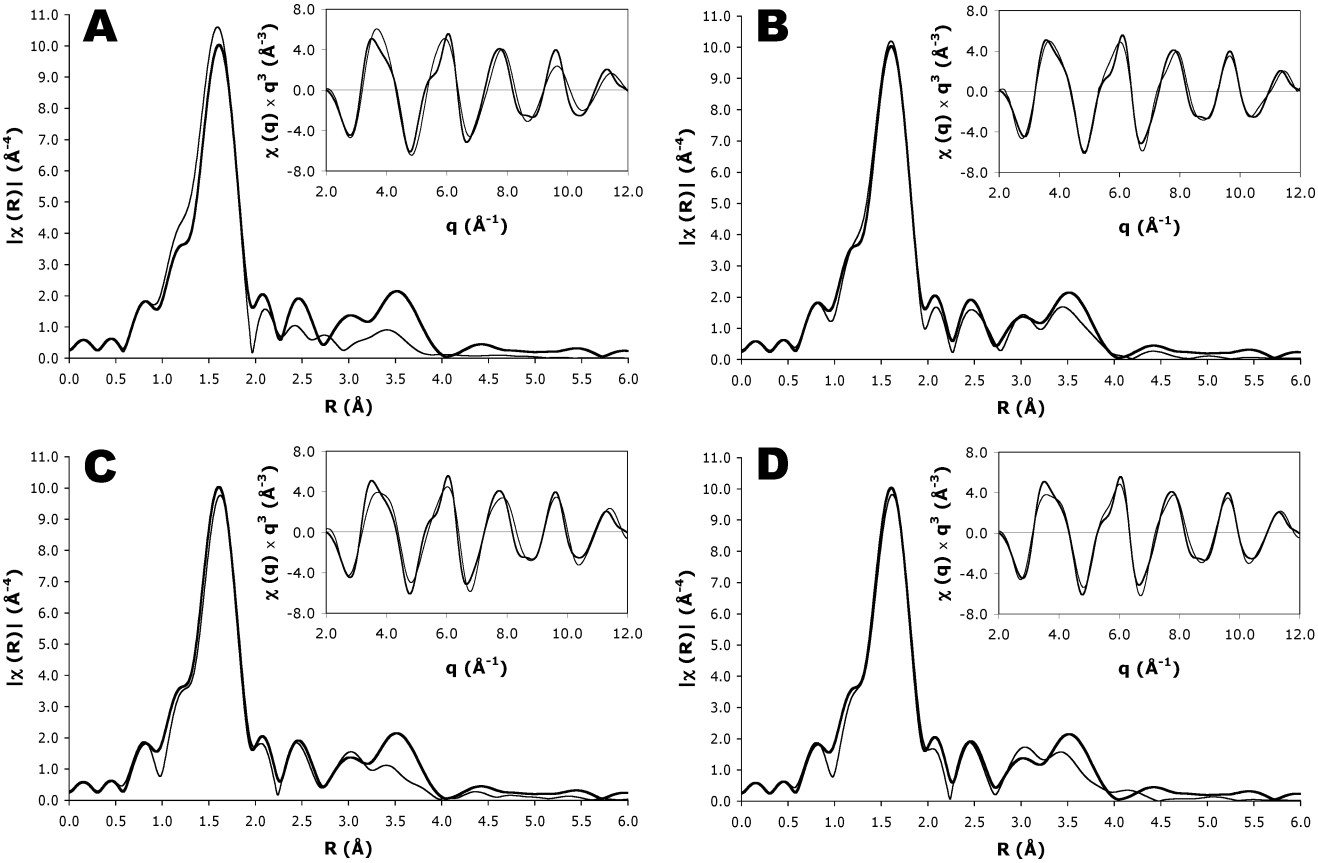

FIGURE 5: Magnitude of the Fourier transform of the k^3-weighted $\chi(k)$ data (thick line) and best-fit (thin line) for *Bp*UreE−Ni_2. In each panel, the fit corresponds to the best structural template belonging to the **A**, **B**, **C**, and **D** groups shown in Figure 2 (templates **A1**, **B2**, **C4**, and **D1**). The back-transformed signal in *q*-space is shown in the inset.

transforms (reported as insets in each panel of Figure 5) show a poor fit in the characterization of the shape of the camelback oscillation located at about 6.0 $Å^{-1}$. On the basis of the obtained parameters (Table 1), it is possible to exclude templates **A** and **C**, while templates **B** and **D** show similar statistics.

To try to improve the fits while taking into consideration the stoichiometry of nickel-binding data that indicate the presence of 2 Ni^{2+} ions bound to the full metal-loaded *Bp*UreE, we tested the effect of including, in the templates, a bridging Ni−O−Ni moiety. In Figure 2, all the possible templates are reported (indicated by an asterisk) obtained by adding the −ONi fragment to the mononuclear sites tested thus far. Figure 6 reports the experimental Fourier-transformed EXAFS data compared with the best-simulated Fourier transforms for templates including one −ONi group and zero (**A***), one (**B***), two (**C***), and three (**D***) histidines. Inclusion of the −ONi fragment in template **A** (**A***), improves the statistical parameters of the fit ($\chi_v^2(R)$ decreases from 20.1 to 15.6), but the peaks located at about 2.5, 3.0, and 3.5 Å are still poorly simulated. Insertion of the −ONi group in templates **B** does not produce significant variations in the statistical parameters of the fits (the $\chi_v^2(R)$ values for the **B*** templates range from 9.3 to 10.5, almost the same as observed for the **B** models). In contrast, the addition of the −ONi fragment in templates **C** and **D** yields significant improvements. In particular, the $\chi_v^2(R)$ for templates **C*** drops to 3.7−7.8, while that for templates **D*** ranges from 6.3 to 9.1. The best template belonging to the **C*** group (**C5a***, $\chi_v^2(R) = 3.7$, *R*-factor = 1.16%) allows us to obtain an accurate fit of the peaks at 2.0, 2.5, and 3.0 Å, and a very good approximation of the peak at 3.5 Å (Figure 6). The best template of the **D*** group (**D10a***, $\chi_v^2(R) = 5.9$, *R*-factor = 1.87%) shows a quality of fit for the peaks at 2.0, 2.5, and 3.5 Å, similar to that found for the **C5a*** structure, but largely overestimates the peak at 3.0 Å.

A general comparison of the results reported in Table 1 and Figures 5 and 6 allows us to exclude, for the structure of the nickel-binding site of *Bp*UreE−Ni_2, the possibilities given by templates **A**, **B**, **C**, and **D**. Therefore, the presence of a Ni−O−Ni moiety is strongly supported by this analysis, and is not a mere result of improving the statistics (and in particular the *R*-factor) by increasing the number of fitted parameters (by the addition of the −ONi fragment). Indeed, the drastic decrease of the reduced χ^2 value ($\chi_v^2(R)$), a statistic probe that takes into account the number of degrees of freedom in the fit, is a clear indication that the improvement brought about by the presence of the Ni−O−Ni moiety is statistically significant. Among the possible templates that include this moiety, the case represented by the **C*** group provides templates showing the best statistics. The best structure is found in the case of the **C5a*** template, which features a Ni(O_3)-*cis*-(His-Nϵ)(His-Nϵ)-ONi metal binding site. In this model, the Ni−O and Ni−N distances found by IFEFFIT are, as expected, in the 2.0−2.1 Å range, with acceptable Debye−Waller factors (see Table 1). The Ni−O−Ni angle selected as best value by the simplex algorithm implemented in the calculation is 114.9° with a Ni−Ni distance of 3.4 Å.

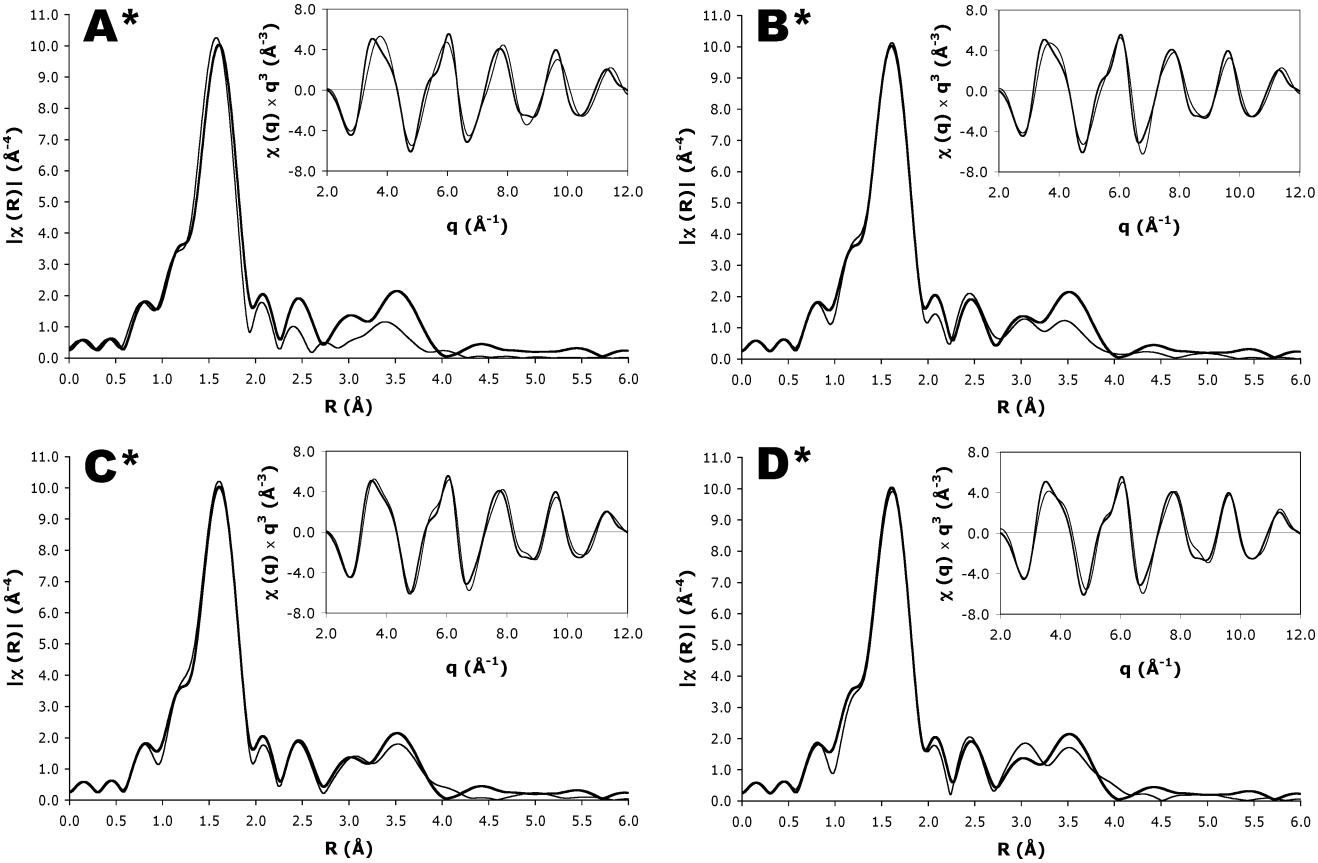

FIGURE 6: Magnitude of the Fourier transform of the k^3-weighted $\chi(k)$ data (thick line) and best-fit (thin line) for *Bp*UreE−Ni_2. In each panel, the fit corresponds to the best structural template belonging to the **A***, **B***, **C***, and **D*** groups shown in Figure 2 (templates **A1***, **B2a***, **C5a***, and **D10b***). The back-transformed signal in *q*-space is shown in the inset.

DISCUSSION

In the past few years, a plethora of functional and structural studies has provided the view that UreE is a metallochaperone in the urease assembly system in vivo, delivering the necessary Ni^{2+} ions into the enzyme active site without incurring metal-induced cell toxicity pathways. However, several incongruent, partial, or erroneous experimental data analyses failed to provide definitive answers to the question of the number of metal ions delivered at each step of the activation, and of the molecular details of the metal ion uptake and release processes involved. In the present study, the use of EXAFS spectroscopy coupled to metal titration analysis provides novel information on the metal binding stoichiometry and coordination properties of *Bp*UreE, overcoming some limitations of X-ray crystallography, and giving a more detailed elucidation of the metal site environment in the fully metal-loaded protein.

The titration of *Bp*UreE performed using Ni^{2+} ions indicates that the homodimeric protein is capable of binding two metal ions. The homodimeric nature of UreE, together with the binding of two metal ions per functional dimer, imposes strict constraints to the topology of the metal-binding sites, and the only two possible models are summarized in Scheme 1. The first model implies that the two binding sites are identical and symmetrically placed around the binary axis passing through the interface that involves the C-terminal domains, as determined by X-ray crystallography (see Figure 1). In this case, the nonhomogeneous binding of the two Ni^{2+} ions ($K_{D1} = 1.4 \pm 0.2$ μM and $K_{D2} = 25 \pm 6$ μM) is interpreted as due to the presence of negative cooperativity, suggesting that the two identical binding sites are close to each other, with the binding of the first ion that decreases the affinity of Ni^{2+} for the second, symmetric site. On the other hand, the second model implies two structurally different binding sites. The derived dissociation constants, $K_{D1} = 0.7 \pm 0.1$ μM and $K_{D2} = 50 \pm 12$ μM, would reflect the intrinsically distinct affinities of the two binding sites, a direct consequence of the different ligand environments.

*Bp*UreE is characterized by the presence of one fully conserved histidine per monomer (His^{100}) (*24*), identified as the residue involved in the binding of Zn^{2+} and Cu^{2+} in the crystal structures of *Bp*UreE (*27*) and *Ka*UreE (*26*), respectively. *Bp*UreE also possesses two additional histidine residues, His^{145} and His^{147}, in the C-terminal pendant arm of each monomer, found disordered in the crystal structures of *Bp*UreE and *Ka*UreE. The total number of histidine residues in the proximity of the putative metal binding site, close to His^{100}, is therefore six. The analysis of the XANES and EXAFS regions of the XAS spectrum, together with a fit of the experimental data using several possible structural models, supports an average coordination shell made of two histidines for each Ni^{2+}-bound *Bp*UreE. Therefore, overall, four histidine residues are coordinated to the metal ions. These residues could be arranged in a 2 + 2, 3 + 1, or 4 + 0 manner, all consistent with the average number of two His bound to each nickel atom. The 3 + 1 option can be excluded, as it would violate the symmetry of the homodimeric system. To distinguish between the 2 + 2 and the 4 + 0 options, we carried out a Bond Valence Sum (BVS) analysis (*65*, *66*) to the best structure obtained (**C5a***). The

Scheme 3

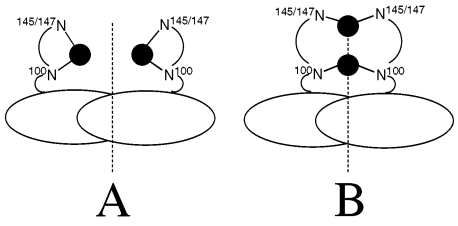

2 + 2 option yields +2.05 as the calculated oxidation state of the Ni ion, while the 4 + 0 option yields +2.36, a value that is largely different from the known +2 oxidation state of nickel. This analysis supports the 2 + 2 option as the best possible for *Bp*UreE. It may be also important to notice that a Ni^{2+} center coordinated by four histidines is yet to be observed in proteins.

The analysis of residues conservation (*24*), mutagenesis studies (*21*, *25*), as well as the available crystallographic structures (*26*, *27*), clearly indicated that His^{100} is involved in metal coordination and is essential for the activity of UreE. For this reason, we are inclined to assume that the two His^{100} residues (one from each monomer) are two of the four imidazole ligands also in the fully loaded *Bp*UreE−Ni_2. The additional two histidines necessary to complete the nickel coordination shell may derive from either His^{145} or His^{147}. According to this view, it is possible to reinterpret the two possible models described in Scheme 1 as described by Scheme 3 .

Consistently with Scheme 3A, each nickel may be coordinated to His^{100} and His^{145}/His^{147}. In this case, a symmetric coordination environment would be built around the two Ni^{2+} ions. The second model, described by Scheme 3B, presupposes the presence of two different metal-binding sites: one Ni^{2+} ion would be bound to two His^{100}, one from each monomer, while the other Ni^{2+} ion would be bound to two histidines (His^{145} or His^{147} in the case of *Bp*UreE), one from each C-terminus fragment found in the monomer.

To provide insights into the coordination environment of the nickel ions in fully loaded *Bp*UreE, we have attempted an analytical methodology that allows the exploration of the compatibility of a large number of biochemically sensible three-dimensional models with experimental EXAFS data. For each structural model, a theoretical signal was calculated that was fit to the experimental spectrum using a small number of parameters as compared to the information contained in the data. In some pertinent cases, a Simplex minimization algorithm was used to guide the exploration of the conformational parameter space, in this way, increasing the speed of the search for the model that would statistically best fit the experimental data. The calculation of the theoretical signal for each tested model takes advantage of the modern developments of EXAFS theory and, in particular, the possibility to explicitly include the multiple scattering pathways of the photoelectron, which depend on the 3D geometry of the active site. In this way, the pathways involving scattering between groups of atoms belonging to different metal ligands can be accounted for. This kind of approach should in principle take into consideration vibrational effects, often described in terms of the EXAFS Debye−Waller factors, which depend on the mean square variation of the path lengths for all multiple-scattering pathways. The large number of these factors renders impossible their inclusion as floating parameters without exceeding the limited information content of the data. A solution proposed for this problem is the calculation of the Debye−Waller factors using density functional theory (*67*−*69*), but this approach is, at present, not practical due to the length of the required calculations for each hypothetical model (*70*). A viable approach to the Debye−Waller factor problem in the multiple scattering fitting of biological EXAFS data has been recently proposed (*70*), which entails the use of conventional minimization algorithms able to map out the parameter space and to select the best model according to the best goodness-of-fit. This was the approach followed in the present study and involved the use of plausible estimates for the Debye−Waller factors, on a group-by-group basis (*69*), in this way limiting the number of floating parameters. The model that we found to statistically best reproduce the experimental EXAFS signal, among the many that were tested here, features the presence of a $(His)_2Ni-O-Ni(His)_2$ moiety. In principle, we cannot exclude that other structures for the nickel center could provide better fits to the experimental EXAFS data if the Debye−Waller factor issue were treated rigorously. In this sense, the proposed model cannot be considered as unambiguous in the absence of ever-desired crystallographic evidence, but could be taken as an interesting point for discussion. The presence of this moiety would be consistent with a possible simultaneous transfer of both nickel ions to the active site of urease, with the obvious biochemical advantage of an all-or-nothing reaction. Such model would be appealing especially if one considers the time and energy efficiency of this process, with the required single step that could avoid the cellular toxicity risks associated with multiple steps of UreE−apourease complex formation, energy-coupled Ni^{2+} delivery, and release of the holoenzyme from its chaperone. Under this assumption, a mode for nickel ions delivering from UreE to urease could be envisioned, in which the metal site constitutes a sort of "building block", Ni−O−Ni, transferred intact to the urease active site in a unique step, optimizing the efficiency of the overall process. This idea is not totally new. A similar hypothesis for simultaneous transfer of two nickel ions during the activation process of urease was proposed few years ago by Hausinger et al. only on the basis of nickel-binding stoichiometry (*20*). Additionally, the role of metallo-chaperones in pre-assembling a metal cluster in addition to transfering it into the target protein cluster receptor is well-documented. An example of this is represented by the IscU (or ISU) family of proteins, which serve a key role as scaffolding proteins on which [2Fe-2S] building blocks are assembled prior to transfer to final apo target proteins (*71*). The hypothesis for the pre-assembly of the Ni−O−Ni moiety in UreE would be consistent with the observed metrics of the Ni−O−Ni moiety as derived from the EXAFS analysis. The best value selected for the Ni−O−Ni angle is 114.9°, with a Ni−Ni distance of 3.4 Å, and these values are comparable to those found in the dinuclear Ni site of urease (119.3° and 3.7 Å) (*63*). To make this mechanism a general feature of all UreEs, the presence of at least one histidine near the C-termini, in addition to His^{100}, is required. A recent study has reported the multiple sequence alignment of all the known UreE sequences so far determined (*24*). Indeed, the analysis of these sequences shows that the occurrence

of a histidine residue near the C-termini is always present in all the UreE sequences. Under this assumption, the flexible nature observed for the C-terminal stretches that support His^{145} and His^{147} would have a plausible functional explanation, because it may allow the displacement of a histidine residue from the nickel ions upon protein complex formation and metal core delivery. The additional histidine present in the C-terminal His-X-His motif, when found in the sequence as in the case of *Bp*UreE, may also have a role, facilitating nickel delivering into the urease active site. The negative cooperativity observed for the binding of the two Ni^{2+} ions to *Bp*UreE is, in principle, not consistent with the release of both metals at once. A caveat to this reasoning is that the negative cooperativity could be an intrinsic property of the UreE protein in vitro, while several other considerations may apply in vivo, including the role of the chaperone itself and the acceptor protein in the transfer of the metal ions from one protein to the other within the preformed super-complex between UreE and the apo-urease/UreDFG complex. Indeed, large changes of protein structure and dynamics upon interactions with biological partners are common. An example pertinent to the urease case is represented by UreG, an intrinsically disordered protein (*13*) thought to undergo a disorder-to-order transition upon binding to the other urease chaperone in order to contribute, through catalytic hydrolysis of GTP, to the in vivo assembly of the urease active site (*15*).

ACKNOWLEDGMENT

The authors are thankful to Dr. Wolfram Meyer-Klaucke for assistance in X-ray absorption data collection at EMBL Hamburg and to Dr. Mauro Andrea Cremonini from the University of Bologna and Dr. Bruce Ravel from Argonne National Laboratory for useful discussions.

REFERENCES

1. O'Halloran, T. V., and Culotta, V. C. (2000) Metallochaperones, an intracellular shuttle service for metal ions, *J. Biol. Chem. 275*, 25057−25060.
2. Finney, L. A., and O'Halloran, T. V. (2003) Transition metal speciation in the cell: insights from the chemistry of metal ion receptors, *Science 300*, 931−936.
3. Huffman, D. L., and O'Halloran, T. V. (2001) Function, structure, and mechanism of intracellular copper trafficking proteins, *Annu. Rev. Biochem. 70*, 677−701.
4. Outten, C. E., and O'Halloran, T. V. (2001) Femtomolar sensitivity of metalloregulatory proteins controlling zinc homeostasis, *Science 292*, 2488−2492.
5. Andrews, N. C. (2002) Metal transporters and disease, *Curr. Opin. Chem. Biol. 6*, 181−186.
6. Luk, E., Jensen, L. T., and Culotta, V. C. (2003) The many highways for intracellular trafficking of metals, *J. Biol. Inorg. Chem. 8*, 803−809.
7. Mulrooney, S. B., and Hausinger, R. P. (2003) Nickel uptake and utilization by microorganisms, *FEMS Microbiol. Rev. 27*, 239−261.
8. Ciurli, S., and Mangani, S. (2001) in *Handbook on Metalloproteins* (Bertini, I., Sigel, A., and Sigel, H., Eds.) pp 669−708, Marcel Dekker, New York.
9. Hausinger, R. P., and Karplus, P. A. (2001) in *Handbook of Metalloproteins* (Messerschmidt, A., Huber, R., Poulos, T., and Wieghardt, K., Eds.) pp 867−879, John Wiley & Sons, Chichester, U.K.
10. Lee, M. H., Mulrooney, S. B., Renner, M. J., Markowicz, Y., and Hausinger, R. P. (1992) *Klebsiella aerogenes* urease gene cluster: sequence of ureD and demonstration that four accessory genes (ureD, ureE, ureF, ureG) are involved in nickel metallocenter biosynthesis, *J. Bacteriol. 174*, 4324−4330.
11. Hausinger, R. P. (1997) Metallocenter assembly in nickel-containing enzymes, *J. Biol. Inorg. Chem. 2*, 279−286.
12. Park, I. S., Carr, M. B., and Hausinger, R. P. (1994) In vitro activation of urease apoprotein and role of UreD as a chaperone required for nickel metallocenter assembly, *Proc. Natl. Acad. Sci., U.S.A. 91*, 3233−3237.
13. Zambelli, B., Stola, M., Musiani, F., De Vriendt, K., Samyn, B., Devreese, B., Van Beeumen, J., Turano, P., Dikiy, A., Bryant, D. A., and Ciurli, S. (2005) UreG, a chaperone in the urease assembly process, is an intrinsically unstructured GTPase that specifically binds Zn^{2+}, *J. Biol. Chem. 280*, 4684−4695.
14. Lee, M. H., Mulrooney, S. B., and Hausinger, R. P. (1990) Purification, characterization, and in vivo reconstitution of *Klebsiella aerogenes* urease apoenzyme, *J. Bacteriol. 172*, 4427−4431.
15. Soriano, A., and Hausinger, R. P. (1999) GTP-dependent activation of urease apoprotein in complex with the UreD, UreF, and UreG accessory proteins, *Proc. Natl. Acad. Sci., U.S.A. 96*, 11140−11144.
16. Park, I. S., and Hausinger, R. P. (1995) Evidence for the presence of urease apoprotein complexes containing UreD, UreF, and UreG in cells that are competent for in vivo enzyme activation, *J. Bacteriol. 177*, 1947−1951.
17. Mulrooney, S. B., and Hausinger, R. P. (1990) Sequence of the *Klebsiella aerogenes* urease genes and evidence for accessory proteins facilitating nickel incorporation, *J. Bacteriol. 172*, 5837−5843.
18. Lee, M. Y., Pankratz, H. S., Wang, S., Scott, R. A., Finnegan, M. G., Johnson, M. K., Ippolito, J. A., Christianson, D. W., and Hausinger, R. P. (1993) Purification and characterization of *Klebsiella aerogenes* UreE protein: a nickel binding protein that functions in urease metallocenter assembly, *Protein Sci. 2*, 1042−1052.
19. Brayman, T. G., and Hausinger, R. P. (1996) Purification, characterization, and functional analysis of a truncated *Klebsiella aerogenes* UreE urease accessory protein lacking the histidine-rich carboxyl terminus, *J. Bacteriol. 178*, 5410−5416.
20. Colpas, G. J., Brayman, T. G., McCracken, J., Pressler, M. A., Babcock, G. T., Ming, L.-J., Colangelo, C. M., Scott, R. A., and Hausinger, R. P. (1998) Spectroscopic characterization of metal binding by *Klebsiella aerogenes* UreE urease accessory protein, *J. Biol. Inorg. Chem. 3*, 150−160.
21. Colpas, G. J., Brayman, T. G., Ming, L. J., and Hausinger, R. P. (1999) Identification of metal-binding residues in the *Klebsiella aerogenes* urease nickel metallochaperone, UreE, *Biochemistry 38*, 4078−4088.
22. Soriano, A., Colpas, G. J., and Hausinger, R. P. (2000) UreE stimulation of GTP-dependent urease activation in the UreD-UreF-UreG-urease apoprotein complex, *Biochemistry 39*, 12435−12440.
23. Mobley, H. L. T., Island, M. D., and Hausinger, R. P. (1995) Molecular biology of microbial ureases, *Microbiol. Rev. 59*, 451−480.
24. Musiani, F., Zambelli, B., Stola, M., and Ciurli, S. (2004) Nickel trafficking: insights into the fold and function of UreE, a urease metallochaperone, *J. Inorg. Biochem. 98*, 803−813.
25. Colpas, G. J., and Hausinger, R. P. (2000) In vivo and in vitro kinetics of metal transfer by the *Klebsiella aerogenes* urease nickel metallochaperones, UreE*, *J. Biol. Chem. 275*, 10731−10737.
26. Song, H.-K., Mulrooney, S. B., Huber, R., and Hausinger, R. P. (2001) Crystal structure of *Klebsiella aerogenes* UreE, a nickel-binding metallochaperone for urease activation, *J. Biol. Chem. 276*, 49359−49364.
27. Remaut, H., Safarov, N., Ciurli, S., and Van Beeumen, J. J. (2001) Structural basis for Ni transport and assembly of the urease active site by the metallo-chaperone UreE from *Bacillus pasteurii*, *J. Biol. Chem. 276*, 49365−49370.
28. Mehta, N., Benoit, S., and Maier, R. J. (2003) Roles of conserved nucleotide-binding domains in accessory proteins, HypB and UreG, in the maturation of nickel-enzymes required for efficient *Helicobacter pylori* colonization, *Microb. Pathog. 35*, 229−234.
29. Won, H. S., Lee, Y. H., Kim, J. H., Shin, I. S., Lee, M. H., and Lee, B. J. (2004) Structural characterization of the nickel-binding properties of *Bacillus pasteurii* urease accessory protein (Ure)E in solution, *J. Biol. Chem. 279*, 17466−17472.
30. Ciurli, S., Safarov, N., Miletti, S., Dikiy, A., Christensen, S. K., Kornetzky, K., Bryant, D. A., Vandenberghe, I., Devreese, B., Samyn, B., Remaut, H., and Van Beeumen, J. J. (2002) Molecular characterization of *Bacillus pasteurii* UreE, a metal-binding chaperone for the assembly of the urease active site, *J. Biol. Inorg. Chem. 7*, 623−631.

31. Benini, S., Gessa, C., and Ciurli, S. (1996) *Bacillus pasteurii* urease: an heteropolymeric enzyme with a binuclear nickel active site, *Soil Biol. Biochem. 28*, 819−821.
32. Benini, S., Ciurli, S., Nolting, H. F., and Mangani, S. (1996) X-ray absorption spectroscopy study of native and phenylphosphorodiamidate-inhibited *Bacillus pasteurii* urease, *Eur. J. Biochem. 239*, 61−66.
33. Benini, S., Rypniewski, W. R., Wilson, K. S., Ciurli, S., and Mangani, S. (1998) The complex of *Bacillus pasteurii* urease with β-mercaptoethanol from X-ray data at 1.65 Å resolution, *J. Biol. Inorg. Chem. 3*, 268−273.
34. Benini, S., Rypniewski, W. R., Wilson, K. S., Miletti, S., Ciurli, S., and Mangani, S. (1999) A new proposal for urease mechanism based on the crystal structures of the native and inhibited enzyme from *Bacillus pasteurii*: why urea hydrolysis costs two nickels, *Struct. Folding Des. 7*, 205−216.
35. Benini, S., Rypniewski, W. R., Wilson, K. S., Miletti, S., Ciurli, S., and Mangani, S. (2000) The complex of *Bacillus pasteurii* urease with acetohydroxamate anion from X-ray data at 1.55 Å resolution, *J. Biol. Inorg. Chem. 5*, 110−118.
36. Musiani, F., Arnofi, E., Casadio, R., and Ciurli, S. (2001) Structure-based computational study of the catalytic and inhibition mechanism of urease, *J. Biol. Inorg. Chem. 3*, 300−314.
37. Benini, S., Rypniewski, W. R., Wilson, K. S., Ciurli, S., and Mangani, S. (2001) Structure-based rationalization of urease inhibition by phosphate: novel insights into the enzyme mechanism, *J. Biol. Inorg. Chem. 6*, 778−790.
38. Benini, S., Rypniewski, W. R., Wilson, K. S., Mangani, S., and Ciurli, S. (2004) Molecular details of urease inhibition by boric acid: insights into the catalytic mechanism, *J. Am. Chem. Soc. 126*, 3714−3715.
39. Laemmli, U. K. (1970) Cleavage of structural proteins during the assembly of the head of bacteriophage T4, *Nature 227*, 680−685.
40. Pettifer, R. F., and Hermes, C. (1985) Absolute energy calibration of X-ray radiation from synchrotron sources, *J. Appl. Crystallogr. 18*, 404−412.
41. Ravel, B., and Newville, M. (2005) ATHENA, ARTEMIS, HEPHAESTUS: data analysis for X-ray absorption spectroscopy using IFEFFIT, *J. Synchrotron Radiat. 12*, 537−541.
42. Newville, M., Livins, P., Yacoby, Y., Rehr, J. J., and Stern, E. A. (1993) Near-edge X-ray-absorption fine structure of Pb: a comparison of theory and experiment, *Phys. Rev. B: Condens. Matter Mater. Phys. 47*, 14126−14131.
43. Stern, E. A., and Heald, M. A. (1983) *Basic Principles and Applications of EXAFS*, Vol. 10, North-Holland, Amsterdam, Netherlands.
44. Rehr, J. J., Mustre de Leon, J., Zabinsky, S. I., and Albers, R. C. (1991) Theoretical X-ray absorption fine structure standards, *J. Am. Chem. Soc. 113*, 5135−5140.
45. Rehr, J. J., and Albers, R. C. (1990) Scattering-matrix formulation of curved-wave multiple-scattering theory: application to X-ray-absorption fine structure, *Phys. Rev. B 41*, 8139−8149.
46. Zabinsky, S. I., Rehr, J. J., Ankudinov, A., Albers, R. C., and Eller, M. J. (1995) Multiple scattering calculations of X-ray absorption spectra, *Phys. Rev. B 52*, 2995−3009.
47. Newville, M. (2001) IFEFFIT: interactive XAFS analysis and FEFF fitting, *J. Synchrotron Radiat. 8*, 322−324.
48. Newville, M., Ravel, B., Haskel, D., Rehr, J. J., Stern, E. A., and Yacoby, Y. (1995) Analysis of multiple-scattering XAFS data using theoretical standards, *Physica B 208−209*, 154−155.
49. Case, D. A., Pearlman, D. A., Caldwell, J. W., Cheatham, T. E., III, Ross, W. S., Simmerling, C. L., Darden, T. A., Merz, K. M., Stanton, R. V., Cheng, A. L., Vincent, J. J., Crowley, M., Tsui, V., Radmer, R. J., Duan, Y., Pitera, J., Massova, I., Seibel, G. L., Singh, U. C., Weiner, P. K., and Kollman, P. A. (1999), University of California, San Francisco, CA.
50. Cornell, W. D., Cieplak, P., Bayly, C. J., Gould, I. R., Merz, K. M., Jr., Ferguson, D. M., Spellmeyer, D. C., Fox, T., Caldwell, J. W., and Kollman, P. A. (1995) A second generation force field for the simulation of proteins, nucleic acid, and organic molecules, *J. Am. Chem. Soc. 117*, 5179−5197.
51. Nelder, J. A., and Mead, R. (1965) A simplex method for function minimization, *Comput. J. 7*, 308−313.
52. Kay, L. E., Torchia, D. A., and Bax, A. (1989) Backbone dynamics of proteins as studied by ^{15}N inverse detected heteronuclear NMR spectroscopy: application to *Staphylococcus* nuclease, *Biochemistry 28*, 8972−8979.
53. Palmer, A. G. I., Skelton, N. J., Chazin, W. J., Wright, P. E., and Rance, M. (1992) Suppression of the effects of cross-relaxation between dipolar and anisotropic chemical shift relaxation mechanisms in the measurement of spin−spin relaxation rates, *Mol. Phys. 75*, 699−711.
54. Barbato, G., Ikura, M., Kay, L. E., Pastor, R. W., and Bax, A. (1992) Backbone dynamics of calmodulin studied by ^{15}N relaxation using inverse detected two-dimensional NMR spectroscopy: the central helix is flexible, *Biochemistry 31*, 5269−5278.
55. Kay, L. E., Nicholson, L. K., Delaglio, F., Bax, A., and Torchia, D. A. (1992) Pulse sequences for removal of the effects of cross correlation between dipolar and chemical shift anisotropy relaxation mechanisms on the measurement of heteronuclear T_1 and T_2 values in proteins, *J. Magn. Reson. 97*, 359−375.
56. Grzesiek, S., and Bax, A. (1993) The importance of not-saturating H_2O in protein NMR: application to sensitivity enhancement and NOE measurements, *J. Am. Chem. Soc. 115*, 12593−12594.
57. Peng, J. W., and Wagner, G. (1992) Mapping of spectral density function using heteronuclear NMR relaxation measurements, *J. Magn. Reson. 98*, 308−332.
58. Goddard, T. D., and Kneller, D. G., University of California, San Francisco, CA.
59. Lee, Y.-H., Won, H.-S., Lee, M.-H., and Lee, B.-J. (2002) Effects of salt and nickel ion on the conformational stability of *Bacillus pasteurii* UreE, *FEBS Lett. 522*, 135−140.
60. Attie, A. D., and Raines, R. T. (1995) Analysis of receptor−ligand interactions, *J. Chem. Educ. 72*, 119−124.
61. Lakowicz, J. R. (1999) *Principles of Fluorescence Spectroscopy*, Plenum Publishing, New York.
62. Colpas, G. J., Maroney, M. J., Bagyinka, C., Kumar, M., Willis, W. S., Suib, S. L., Baidya, N., and Mascharak, P. K. (1991) X-ray spectroscopic studies of nickel complexes, with application to the structure of nickel sites in hydrogenases, *Inorg. Chem. 30*, 920−928.
63. Ciurli, S., Benini, S., Rypniewski, W. R., Wilson, K. S., Miletti, S., and Mangani, S. (1999) Structural properties of the nickel ions in urease: novel insights into the catalytic and inhibition mechanisms, *Coord. Chem. Rev. 190−192*, 331−355.
64. Chance, M. R., Miller, L. M., Fischetti, R. F., Scheuring, E., Huang, W. X., Sclavi, B., Hai, Y., and Sullivan, M. (1996) Global mapping of structural solutions provided by the extended X-ray absorption fine structure ab initio code FEFF 6.01: structure of the cryogenic photoproduct of the myoglobin-carbon monoxide complex, *Biochemistry 35*, 9014−9023.
65. Thorp, H. H. (1992) Bond valence sum analysis of metal−ligand bond lengths in metalloenzymes and model complexes, *Inorg. Chem. 31*, 1585−1588.
66. Liu, W., and Thorp, H. H. (1993) Bond valence sum analysis of metal−ligand bond lengths in metalloenzymes and model complexes. 2. Refined distances and other anzymes, *Inorg. Chem. 32*, 4102−4105.
67. Dimakis, N., Al-Akhras, M. A., and Bunker, G. (1999) Rapid single- and multiple-scattering EXAFS Debye−Waller factor calculations on active sites of metalloproteins, *J. Synchrotron Radiat. 6*, 266−267.
68. Dimakis, N., and Bunker, G. (2001) Chemical transferability of single- and multiple-scattering EXAFS Debye−Waller factors, *J. Synchrotron Radiat. 8*, 297−299.
69. Dimakis, N., and Bunker, G. (2002) Group-fitted ab initio single- and multiple-scattering EXAFS Debye−Waller factors, *Phys. Rev. B 65*, 201103-1−201103-4.
70. Bunker, G., Dimakis, N., and Khelashvili, G. (2005) New methods for EXAFS analysis in structural genomics, *J. Synchrotron Radiat. 12*, 53−56.
71. Mansy, S. S., and Cowan, J. A. (2004) Iron−sulfur cluster biosynthesis: toward an understanding of cellular machinery and molecular mechanism, *Acc. Chem. Res. 37*, 719−725.

BI0601003